Dynamical propagation and growth mechanisms for convectively coupled equatorial Kelvin waves over the Indian Ocean

Adrian J. Matthews*[a]

[a]*Centre for Ocean and Atmospheric Sciences, School of Environmental Sciences and School of Mathematics, University of East Anglia, UK*

Correspondence to: Prof. Adrian Matthews, School of Environmental Sciences, University of East Anglia, Norwich, NR4 7TJ, UK.
a.j.matthews@uea.ac.uk

Convectively coupled equatorial Kelvin waves (CCKWs) are high-impact tropical weather systems that can lead to severe flooding over the Maritime Continent. Here, a vorticity budget for CCKWs over the Indian Ocean is constructed using reanalysis data, to identify the basic mechanisms of eastward propagation and growth. The budget is reasonably well closed, with a small residual/sub-gridscale term. In the lower troposphere, CCKWs behave like strongly modified theoretical equatorial Kelvin waves. Vortex stretching, from the divergence of the Kelvin wave acting on planetary vorticity (the $-fD$ term), is the sole mechanism by which the vorticity structure of a theoretical Kelvin wave propagates eastward. In the lower and middle troposphere, this term is also the key mechanism for the eastward propagation of CCKWs but, due to subtleties in its structure and phasing linked to a combination of modal structures, it also contributes to growth. Unlike in the theoretical Kelvin wave, other vorticity source terms also play a role in the propagation and growth of CCKWs. In particular, vortex stretching from relative vorticity (the $-\zeta D$ term) is the largest source term, and this leads strongly to growth, through interactions between the background and perturbation vorticity and divergence. Horizontal vorticity advection by the background flow contributes to propagation, and also acts to retard the growth of the CCKW. The sum of the source terms in this complex vorticity budget leads to eastward propagation and growth of CCKWs. The structure and vorticity budget of CCKWs in the upper troposphere is quite unlike that of a Kelvin wave, and appears to arise as a forced response to the lower tropospheric structure. The implications for numerical weather prediction and climate simulations are discussed.

Key Words: Equatorial wave; Kelvin wave; vorticity budget; growth rate; eastward propagation; tropical weather system

1. Introduction

Convectively coupled equatorial Kelvin waves (CCKWs) are tropical weather systems that propagate eastward along the equator (Takayabu 1994; Dunkerton and Crum 1995; Wheeler and Kiladis 1999) and cause a typical increase in rainfall rate of 10 mm day^{-1} (Baranowski et al. 2016a). They are one type of a class of convectively coupled equatorial waves (Kiladis et al. 2009). CCKWs have a strong impact on monsoon precipitation (Mekonnen et al. 2009), and are a major component of the envelope of convective systems that make up the active phase of the Madden–Julian Oscillation (MJO; Guo et al. 2014; Haertel et al. 2015; Kikuchi et al. 2018). Indeed, an accurate representation of convectively coupled equatorial waves in a climate model is positively correlated with that model's ability to simulate the MJO accurately (Guo et al. 2015). The passage of CCKWs can strongly modify the underlying diurnal cycle of convection (Sakaeda et al. 2020), and constructive interference from the triggering of the diurnal cycle over successive islands in the Maritime Continent can positively feedback on the development of the CCKWs themselves (Baranowski et al. 2016b).

CCKWs are responsible for high impact weather (Ferrett et al. 2020; Lubis and Respati 2021), including major flooding incidents (Baranowski et al. 2020; Latos et al. 2021). They can be identified and skillfully forecast in real time in atmospheric models (Yang et al. 2021), but also have a significant, possibly two-way interaction with the underlying ocean (Baranowski et al. 2016a, 2017).

Dynamically, CCKWs are generally considered as ~~an adaption~~ a modified version of theoretical, linear, dry equatorial Kelvin waves (Matsuno 1966; Gill 1980), as their variance maxima lie along the dispersion curves of the theoretical waves (Wheeler and Kiladis 1999), and they have at least a superficially similar dynamical structure (Wheeler et al. 2000; Straub and Kiladis 2002; Yang et al. 2007a), with near-zero meridional wind anomalies, and zonal wind anomalies that are a maximum on the equator.

The dynamics of theoretical, linear, dry equatorial Kelvin waves are well understood. It is often assumed that the dynamics of CCKWs are similar, even though key differences in the phasing of the mass (geopotential height) and dynamical (zonal wind) fields between observed "dry" equatorial Kelvin waves and CCKWs have been identified (Roundy 2012).

The purpose of this paper is to establish the dynamical mechanisms for the eastward propagation and growth of CCKWs. In particular, the hypothesis is tested that CCKWs have the same eastward propagation mechanism as theoretical, linear, dry equatorial Kelvin waves. Additionally, theoretical equatorial Kelvin waves are neutral. Hence, how does the structure of CCKWs differ from that of theoretical Kelvin waves to allow them to dynamically grow? A vorticity budget approach will be used, following the successful application of this technique to diagnose the dynamical mechanisms by which transient extratropical waves excite convection along the South Pacific and South Atlantic Convergence Zones (van der Wiel et al. 2015). The dynamical vorticity budget approach presented in this study can be viewed as ~~one half of a full~~ a partial analysis of CCKW mechanisms. A complementary analysis based on the thermodynamic and moisture budgets of CCKWs will be a subject of future study.

Theoretical preliminaries are presented in Section 2, and the data and methodology used are described in Section 3. Section 4 presents detailed results of the CCKW structure and vorticity budget for a single level in the lower troposphere (850 hPa). This analysis is then expanded to further levels in Section 5 to determine the vertical structure of CCKWs. These levels are representative of the: boundary layer (975 hPa); middle troposphere (500 hPa); upper troposphere (200 hPa). Section 6 presents a discussion and conclusions.

2. Theoretical preliminaries

2.1. Vorticity budget

The vorticity equation for flow on a quasi-horizontal pressure level in Cartesian coordinates can be written as

$$\frac{\partial\zeta}{\partial t} = \underbrace{-u\frac{\partial\zeta}{\partial x} - v\frac{\partial\zeta}{\partial y} - \omega\frac{\partial\zeta}{\partial p}}_{\substack{\text{advection of}\\ \text{relative vorticity}}} \quad \underbrace{-\zeta D - fD}_{\text{vortex stretching}} \quad \underbrace{-\beta v}_{\substack{\text{advection of}\\ \text{planetary vorticity}}} \quad \underbrace{-\left(\frac{\partial\omega}{\partial x}\frac{\partial v}{\partial p} - \frac{\partial\omega}{\partial y}\frac{\partial u}{\partial p}\right)}_{\text{tilting/twisting}}, \tag{1}$$

where: x and y are the horizontal coordinates (eastward and northward distance) from an origin on the equator at $y = 0$; p is the vertical pressure coordinate; t is time; u, v and ω are the components of the three-dimensional velocity vectory; ζ is relative vorticity; D is horizontal divergence; f is planetary vorticity, and β is the northward gradient of planetary vorticity, $\beta = df/dy$.

The vorticity tendency on the left hand side of Equation 1 is balanced by the sum of several vorticity source terms on the right, and can be considered as a vorticity budget when applied to a specific system, such as a theoretical equatorial Kelvin wave, or an observed CCKW. In this paper, we consider the vorticity distribution $\zeta(x, y)$ of our system at a given time. The spatial (x, y) structures of the vorticity source terms and their positions relative to the vorticity distribution can then be used to diagnose the propagation mechanism(s) of the system.

2.2. Theoretical linear equatorial Kelvin wave

The kinematic part of the theoretical linearised (small amplitude) equatorial Kelvin wave solution to the shallow water equations in a resting atmosphere (zero background flow) on an equatorial β-plane $f = \beta y$ (Gill 1982) is

$$u(x, y, t) = u_0\, e^{-\beta y^2/2c_e}\, \mathrm{Re}[e^{ik(x - c_e t)}]\,, \tag{2}$$

$$v(x, y, t) = 0\,, \tag{3}$$

where: u_0 is the amplitude of the zonal wind perturbation on the equator; c_e is a positive constant originating from the separation constant when the (x, y, t) dependence in the shallow water equations was separated from the p dependence in the vertical structure equation; k is the wavenumber in the eastward direction, and $\mathrm{Re}[X]$ denotes the real part of $[X]$. From hereon, the real part of any complex exponential is implicitly assumed. It can be seen that c_e corresponds to the (eastward) phase speed of the theoretical Kelvin wave, and also determines the trapping scale

$$y_0 = \sqrt{\frac{2c_e}{\beta}} \tag{4}$$

in the Gaussian y structure.

The relative vorticity of the theoretical Kelvin wave is then

$$\zeta = \frac{\partial v}{\partial x} - \frac{\partial u}{\partial y} = -\frac{\partial u}{\partial y} = \zeta_0\, y e^{-\beta y^2/2c_e}\, e^{ik(x - c_e t)}\,, \tag{5}$$

where $\zeta_0 = \beta u_0/c_e$, and the divergence of the theoretical Kelvin wave is

$$D = \frac{\partial u}{\partial x} + \frac{\partial v}{\partial y} = \frac{\partial u}{\partial x} = \frac{k c_e \zeta_0}{\beta}\, e^{-\beta y^2/2c_e}\, e^{i[k(x - c_e t) + \frac{\tau}{4}]}\,, \tag{6}$$

where $\tau = 2\pi$ radians corresponds to one "turn" or one full cycle (Abbott 2012). Hence $\frac{\tau}{4}$ $(= \frac{\pi}{2})$ in Equation 6 represents a quarter of a cycle, which is made clearer using the τ notation. For this small amplitude flow on a resting atmosphere, all terms in the vorticity equation (Equation 1) that are nonlinear (quadratic) in perturbation quantities are negligible: advection terms; vortex stretching from the Kelvin wave divergence acting on its own relative vorticity $(-\zeta D)$; tilting/twisting terms. Advection of planetary vorticity $(-\beta v)$ is linear, but as $v = 0$ for the Kelvin wave, this term is also zero. Hence, the vorticity budget reduces to just a single source term: vortex stretching from the Kelvin wave divergence acting on planetary vorticity $(-fD)$. This is confirmed by examination of the vorticity and divergence solutions (Equations 5 and 6):

$$\frac{\partial\zeta}{\partial t} = -fD = k c_e \zeta_0\, y e^{-\beta y^2/2c_e}\, e^{i[k(x - c_e t) - \frac{\tau}{4}]}\,. \tag{7}$$

The basic Gaussian structure of the zonal wind anomalies of Equation 2 are readily apparent (black contours and wind vectors in Figure 1), with a maximum on the equator that decays polewards into both hemispheres with trapping scale y_0. For the parameters used here ($\beta = 2.29 \times 10^{-11}$ m^{-1} s^{-1}, $c_e =$ 5.5 m s^{-1}), the trapping scale is $y_0 = 690$ km. Note that although the theoretical Kelvin wave has been calculated in Cartesian coordinates, it is then transformed and replotted here in spherical Earth coordinates to allow for comparison later with diagnostics of observed CCKWs. The transformation is through a Mercator projection which introduces little distortion in the tropics. Only the region over the "Indian Ocean" is plotted here, which covers approximately 1.5 wavelengths for this sample wave. There is a maximum in the zonal wind at approximately 67°E.

The vorticity structure is also readily apparent, as a dipole (from the $y\exp[-(y/y_0)^2]$ part of Equation 5) of cyclonic shear alongside the zonal wind anomaly at 67°E: positive in the Northern Hemisphere and negative in the Southern Hemisphere (colour shading in Figure 1). To the west and east of these structures (at approximately 42°E and 92°E, respectively), there are negative zonal wind anomalies and dipoles of anticyclonic shear, in the opposite phases of the wave; the chosen value of the zonal wavenumber parameter is $k = 1.08 \times 10^{-6}$ m^{-1}, corresponding to a wavelength of 5820 km.

Finally, the divergence structure of Equation 6 can be seen in the colour line contours in Figure 1. This has the same basic Gaussian structure in y as the zonal wind field. At 80°E, there is a region of negative divergence corresponding to the convergence between the westerly winds to the west and the easterly winds to the east. Similarly, there is a region of positive divergence a half wavelength to the west, at 55°E. Note that the divergence structure is a quarter cycle out of phase with the zonal wind and vorticity structures.

The dynamical mechanism of the eastward propagation of the theoretical Kelvin wave can now be seen. Focusing first on the positive vorticity anomaly in the Northern Hemisphere centred at 5°N, 67°E, there is a negative divergence anomaly a quarter wavelength to the east, at 80°E (Figure 1). As f is positive in the Northern Hemisphere, the vortex stretching term $-fD$ is also positive. Hence we have a *positive* vorticity tendency to the *east* of a positive vorticity anomaly, and therefore the local vorticity structure propagates *eastward*. This is shown explicitly in Figure 2. The negative vorticity anomaly in the Southern Hemisphere at 5°S, 67°E still has a negative divergence anomaly a quarter wavelength to the east, at 80°E. However, f is now negative, and the vortex stretching term $-fD$ is now negative. Hence, here we have a *negative* vorticity tendency to the *east* of a negative vorticity anomaly, and again the local vorticity structure propagates *eastward*. This relationship is repeated throughout the whole theoretical Kelvin wave structure, and hence the wave propagates eastward.

We note in passing that a similar argument can be applied to the thermodynamical part of the Kelvin wave. The dynamical and thermodynamical structures are related through thermal wind balance (geostrophic plus hydrostatic balance). Geopotential height anomalies are in phase with zonal wind anomalies through geostrophic balance. Assuming a simple two-layer (first baroclinic mode) vertical structure for convenience, then through hydrostatic balance the mid-level temperature anomalies are out of phase with the lower-level geopotential and zonal wind anomalies, and in phase with the upper-level geopotential and zonal wind anomalies. Hence, there is a mid-tropospheric cold anomaly above the low-level westerly zonal wind anomalies (at approximately 67°E in Figure 1). The low-level convergence a quarter cycle to the east (80°E in Figure 1) leads to upward vertical velocity above it through mass conservation. The adiabatic cooling due to this ascent (i.e., a *negative* temperature tendency) is then a quarter wavelength to the *east* of the *negative* temperature anomaly in the Kelvin wave, again leading to eastward propagation of the entire wave. We also note that diabatic heating from convection and radiation in observed CCKWs will likely go a long way toward explaining some of the discrepancies from the adiabatic theory presented here. However, in this paper we concentrate only on the dynamical (vorticity) structure of the wave.

In summary, the vorticity budget for a theoretical linear equatorial Kelvin wave in a resting atmosphere is straight forward, with vortex stretching due to convergence/divergence of the zonal wind anomalies providing a vorticity source term that is phase shifted by a quarter cycle compared with the vorticity anomaly, leading to eastward propagation. This quadrature relationship also ensures that the wave is “neutral”; it neither grows nor decays with time. However, there is no such guarantee or even expectation that such a simple relation will exist for an observed CCKW. In the next section we devise a methodology to diagnose how multiple vorticity source terms can affect the propagation and growth of observed CCKWs.

2.3. *Vorticity budget of observed equatorial Kelvin wave*

We allow for a growing/decaying and propagating wave by introducing a complex phase speed $c = c_r + ic_i$, by setting

$$\zeta = \zeta_0\, g(y)\, e^{ik(x-ct)} = \zeta_0\, g(y)\, e^{kc_i t}\, e^{ik(x-c_r t)}\,, \tag{8}$$

where

$$g(y) = ye^{-\beta y^2/2c_e}\,. \tag{9}$$

Such a structure grows exponentially with growth rate kc_i, and propagates eastward with propagation speed $c = c_r$. We note that

$$\frac{\partial \zeta}{\partial t} = (c_i - ic_r)k\zeta\,. \tag{10}$$

We then have a total source S for the vorticity tendency that has the same x-wavenumber and y structure as ζ, but phase shifted by an angle θ (towards positive x, i.e., to the east) such that

$$\frac{\partial \zeta}{\partial t} = S = re^{-i\theta}kc_e\zeta\,, \tag{11}$$

where here, c_e is calculated from a best-fit Gaussian structure to $g(y)$ in Equation 9. Then, equating the real and imaginary parts of Equations 10 and 11, we find

$$c_i = c_e r\cos\theta; \quad c_r = c_e r\sin\theta\,. \tag{12}$$

The part of the source that is in phase with the ζ structure contributes to the growth, and the part that is in quadrature contributes to the phase propagation.

For the theoretical linear Kelvin wave in Section 2.2, the source term is simply vortex stretching from planetary vorticity

$$S = -fD\,, \tag{13}$$

and using Equation 7 we find

$$r = 1; \quad \theta = \frac{\tau}{4}\,, \tag{14}$$

and

$$c_r = c_e; \quad c_i = 0\,. \tag{15}$$

Hence the vorticity source is perfectly in quadrature with the vorticity perturbation, consistent with a neutral wave propagating at theoretical phase speed c_e.

For our observed CCKW, we can diagnose its theoretical phase speed c_e from the y-structure of its u-wind perturbation (Equation 9). However, the total source will likely not have a perfect quadrature phase shift to the east ($\theta = \tau/4$), and the wave will likely actually have a modified phase speed and a non-zero growth rate, dependent on the values of r and θ from Equation 11, and the subsequent c_i and c_r values from Equation 12.

Furthermore, the total source term will contain contributions from all of the terms on the right hand side of the vorticity budget (Equation 1), as

$$S = \sum_{j=1}^{n} S_j\,, \tag{16}$$

where each individual source term can also be written as a complex exponential

$$S_j = r_j e^{-i\theta_j} c_e k\zeta\,. \tag{17}$$

We note that $r \neq \sum r_j$, and $\theta \neq \sum \theta_j$. For the observed CCKW, we calculate the values of r_j and θ_j for each source term S_j (from composite maps of the relevant structures). Adapting Equation 12, we can then calculate an effective growth rate kc_{ij} and propagation speed c_{rj} for the wave induced by each individual source term. The dependence on growth and propagation on the value of the phase difference θ between the vorticity anomaly and a vorticity source term is summarised in Table 1.

An alternative approach to diagnosing growth or decay is to use enstrophy, E, defined here as the mean of the vorticity anomaly squared over a spatial domain R,

$$E = \frac{1}{R} \iint_R \zeta'^2 \, dx \, dy \, . \tag{18}$$

If the vorticity equation (Equation 1) is multiplied by the vorticity anomaly, then using

$$\frac{\partial}{\partial t} \left(\zeta'^2 \right) = 2\zeta' \frac{\partial \zeta}{\partial t} \, , \tag{19}$$

the enstrophy equation can be formed,

$$\frac{\partial E}{\partial t} = \frac{2}{R} \iint_R \zeta' S \, dx \, dy = \frac{2}{R} \sum_{j=1}^{n} \iint_R \zeta' S_j \, dx \, dy \, . \tag{20}$$

If the system can be described by a simple sinusoidal wave as in Section 2.2, the sign of the enstrophy tendency is determined by the phase difference between the vorticity anomaly and its source term(s). If they are in perfect quadrature, as in the theoretical equatorial Kelvin wave, then the covariance between the vorticity anomaly and the source term is zero, and enstrophy tendency is zero, consistent with a neutral, propagating wave. However, if the vorticity anomaly and the source term have a phase difference less than a quarter cycle (positive covariance), then the enstrophy tendency is positive and growth of the wave occurs. The end member of this set is when there is zero phase difference and maximum covariance of the vorticity anomaly and the source term; this leads to maximum growth but zero propagation speed. If the vorticity anomaly and the source term have a phase difference greater than a quarter cycle (negative covariance), then the enstrophy tendency is negative and the wave decays. These enstrophy calculations and interpretations are also valid if the system cannot be described by a simple sinusoidal wave.

Finally, we note that the enstrophy tendency is essentially the spatial covariance between the vorticity anomaly and a vorticity source term. We can normalise this by dividing by the (spatial) standard deviations of the vorticity anomaly field σ_ζ and the source term field σ_S, to produce a spatial correlation coefficient r_j, where

$$r_j = \frac{1}{\sigma_\zeta \sigma_{S_j}} \iint_A \zeta' S_j \, dx \, dy \, . \tag{21}$$

To clarify, the area integrals in Equations 18, 20 and 21 are calculated from the actual composite maps described in Section 3.2, rather than from any idealised fitted functions.

3. Data and methodology

3.1. Data

The existence and location of observed CCKWs were determined using precipitation data from the Tropical Rainfall Measuring Mission (TRMM) 3B42 product (Huffman et al. 2007). The data used were on a $0.25^\circ \times 0.25^\circ$ grid over the tropics, over the 21-year period from 1 January 1998 to 31 December 2018, with a 3-hour time resolution.

The vorticity budget was determined from the zonal, meridional and vertical wind components, and divergence and vorticity at selected pressure levels from the European Centre for Medium Range Weather Forecasts (ECMWF) ERA-interim reanalysis product (Dee et al. 2011). The data used were on a global reduced Gaussian grid, with 512 equally spaced (approximately 0.70°) longitudes, and 256 Gaussian spaced (again, approximately 0.70°) latitudes. The data were extracted for the same period as the TRMM data, and have a 6-hour time resolution.

3.2. CCKW analysis

CCKWs are generally diagnosed based on one of two complementary methods, both of which rely on the similarity between CCKWs and theoretical equatorial Kelvin waves. The first method (Wheeler and Kiladis 1999) picks out CCKWs based on their equatorially averaged *convective* (cloudiness or precipitation) structure. It is based on a two-dimensional filter in zonal wavenumber–frequency space, designed to extract only those signals that have equivalent depths (with associated phase speeds) in the range over which significant Kelvin wave variance is observed. Other related approaches have also diagnosed CCKWs through the wavenumber–frequency characteristics of their convective signals (Zagar et al. 2005; Roundy and Schreck 2009).

The second method (Yang et al. 2003) also uses wavenumber–frequency filtering, but diagnoses CCKW waves by projecting the latitudinal structure of a theoretical equatorial Kelvin wave onto *dynamical* fields, such as the zonal wind. Again, other studies have used variants of this approach (Gehne and Kleeman 2012; Kikuchi 2014). Finally, a related method has been recently developed to extract Kelvin waves in the upper troposphere and stratosphere based on projections onto a three-dimensional normal mode expansion of the linearised primitive equations (Blaauw and Zagar 2018).

The purpose of this study is to examine the dynamical propagation and growth mechanisms of CCKWs. Hence, CCKWs are diagnosed here based on their *convective* structure (following the framework of Wheeler and Kiladis 1999), rather than based on their *dynamical* structure (following the framework of Yang et al. 2003), so as not to predetermine the dynamical structure of the CCKWs that will then be further analysed.

The method of Baranowski et al. (2016a) was used to isolate the individual CCKW events and their trajectories. This method builds on the methodology of Wheeler and Kiladis (1999). Full details can be found in Baranowski et al. (2016a), and are summarised here. First, the TRMM precipitation data were averaged over the equatorial belt (2.625°S–2.625°N) to create a two-dimensional longitude–time data set (essentially a Hovmöller diagram).

Using a two-dimensional Fast Fourier Transform (FFT), this data set was then filtered in the wavenumber–frequency domain for equatorial Kelvin waves, following the methodology of Wheeler and Kiladis (1999). This filtering only passed eastward-propagating waves with phase speeds in the range 5–30 m s^{-1} (corresponding to equivalent depths H in the range 2.55–91.7 m, where $c^2 = gH$). Individual CCKWs typically have phase speeds in the range 10–17 m s^{-1} (Yang et al. 2007b), but due to their sporadic nature, CCKW variance spills out into the wider wavenumber–frequency range. Additionally, absolute caps were placed in wavenumber and frequency space, such that only zonal planetary wavenumbers 1–14 and only frequencies corresponding to the 2.5–30 day period were passed. This excluded signals from other systems, such as the lower frequency MJO and higher frequency inertio–gravity waves, from contaminating the analysis.

Local temporal maxima (above a pre-determined threshold of 0.15 mm hr^{-1}) in the CCKW-filtered Hovmöller precipitation data set were then used to identify the trajectories of individual CCKW events. Finally, the trajectories were pruned at their western (genesis) and eastern (termination) ends, to counter the effect of the wavenumber–frequency filtering that tends to over extend the trajectories, when compared with the raw, unfiltered precipitation data. Each final trajectory consists of a sequence of paired longitude and time values. The first pair corresponds to the western (genesis) end, and the last pair corresponds to the eastern (termination) end.

Lagged composites were then constructed. First, a crossing longitude was specified, and the date and time of all CCKW trajectories that passed this crossing longitude was noted. For this study, we used a crossing longitude of 75°E in the central Indian Ocean, which led to 122 selected CCKW events, with an associated crossing time for each event. The central Indian Ocean was chosen as this sector has the highest number of CCKW events (Baranowski et al. 2016a), and as a large ocean basin it is remote from any confounding effects of land-sea contrasts and topography that might be found over, for example, the Maritime Continent. Lagged composites of any variable of interest were then calculated, as the lagged mean over all the 122 crossing times.

To illustrate this, the lagged composites of TRMM precipitation anomalies are shown in Figure 3. By design, there is a region of positive precipitation anomalies at zero lag, around the crossing longitude at 75°E (Figure 3b). This anomaly propagates eastward with time at a phase speed of approximately 9 m s^{-1}, being centred at 71°E at lag -1 day (Figure 3b), and at 89°E at lag 1 day (Figure 3c). Here, the TRMM data used in the compositing have not been wavenumber–frequency filtered for CCKWs. Only the seasonal cycle (time mean plus first six annual harmonics) has been subtracted before compositing. Hence, the clean, coherent signals in Figure 3 with maximum anomalies of 25 mm day^{-1}, support the robustness of the CCKW event extraction technique. However, the lagged composites of the dynamical fields from the ERA-Interim data shown later (e.g., zonal wind, vorticity, etc.) were constructed from wavenumber–frequency filtered data, to increase the signal-to-noise ratio.

3.3. *Vorticity budget analysis*

To calculate the CCKW vorticity budget, 6-hourly global fields of all the individual terms in Equation 1 (e.g., $-u\partial\zeta/\partial x$) were first constructed from ERA-Interim velocity, divergence and vorticity fields. The horizontal derivatives were calculated in spectral space using the Windspharm library of Dawson (2016). The vertical (pressure) derivatives were calculated using a weighted mean of forward and backward differences, to take account of any non-equal spacing between pressure levels (Veldman and Rinzema 1992). The time derivatives (for the vorticity tendency $\partial\zeta/\partial t$ term) were calculated by centred differences. Finally, the 6-hourly global fields of the vorticity budget terms were then wavenumber-frequency filtered as described in Section 3.2, before being lag composited in the usual manner.

4. Observed lower tropospheric CCKW structure

The vorticity equation (Equation 1) is valid on a single (pressure) level. Although this study is primarily concerned with the dynamical structure of CCKWs (the “KW” part of CCKWs), the coupling with convection (the “CC” part) is clearly also of great importance. As atmospheric moisture is concentrated in the lower troposphere, this section presents a detailed analysis of CCKW structure and vorticity budget for the 850 hPa level, a standard representative level of the free lower troposphere. The vertical structure is presented in Section 5.

4.1. *Basic dynamical structure*

Before analysing the vorticity budget, the basic dynamical structure of a CCKW is first discussed. Lagged composite maps of the CCKW at 850 hPa (Figure 4) show a close resemblance to the theoretical Kelvin wave structure (Figure 1). The 850 hPa level was chosen as a representative lower tropospheric level, above any confounding effects of the boundary layer. At zero lag (Figure 4b), there is a region of positive (westerly) zonal wind anomalies centred on the equator at approximately 70°E, that exhibits an approximately Gaussian structure with latitude. A (weaker) region of easterly anomalies is situated to the east, with a region of anomalous convergence between them at 80°E. The meridional wind anomalies are very weak compared to the zonal wind anomalies, as evidenced by the east–west orientation of the wind vector anomalies. Associated with the shear of the zonal wind anomalies are vorticity anomalies either side of the equator.

The zonal wind field from the zero-lag composite at 850 hPa in Figure 4b was subjected to a least-squares fit to the function

$$u(x,y) = u_0\, e^{-(y/y_0)^2}\, \cos(kx - \phi), \tag{22}$$

over the domain 60–80°E, 8°S–8°N. The best-fit values of the parameters gave an amplitude of $u_0 = 1.75$ m s^{-1}, a Gaussian trapping scale of $y_0 = 690$ km (corresponding to a theoretical Kelvin wave phase speed of $c_e = 5.5$ m s^{-1}), and a wavenumber of $k = 1.08 \times 10^{-6}$ m^{-1}. Note that the arbitrary values of the parameters of the theoretical Kelvin wave plotted in Figure 1 (u_0, c_e, k, and an arbitrary phase shift ϕ of the whole structure with longitude) were chosen to match those of the CCKW at 850 hPa in Figure 4b.

The main difference between the observed CCKW structure at 850 hPa and the theoretical Kelvin wave is the spatial localisation of the CCKW in the Indian Ocean to within approximately one full wavelength, from the divergence anomaly at 60°E to the divergence anomaly at 100°E. This compares with the endlessly repeated pure wave structure of the theoretical wave. However, over the Indian Ocean domain, the CCKW bears a remarkable resemblance to its theoretical counterpart, especially in the fitting of the Gaussian trapping scale y_0.

The eastward propagation of the CCKW is readily apparent. The convergence centre is at 72°E at lag -1 day (Figure 4a), and 88°E at lag 1 day (Figure 4c), implying a phase speed of 10 m s^{-1}. Note that this actual propagation speed of the CCKW is much higher (by a factor of two) than the theoretical Kelvin wave speed $c_e = 5.5$ m s^{-1} deduced from the Gaussian trapping scale of the CCKW at this level.

4.2. *Vorticity budget: tendency, total source, and residual/sub-gridscale term*

A preliminary analysis of the vorticity budget is presented for the 850-hPa lower tropospheric layer (Fig 5). As expected, the vorticity tendency $\partial\zeta/\partial t$ field (colour shading in Fig 5a) is approximately a quarter cycle out of phase with the vorticity anomaly (line contours in Fig 5a). The phasing is such that, in the Northern Hemisphere, the maximum in vorticity tendency (at approximately 85°E) is to the east of the maximum in the vorticity anomaly (at approximately 73°E), consistent with eastward propagation. Similarly, in the Southern Hemisphere, the minimum in vorticity tendency is to the east of the minimum in the vorticity anomaly, again consistent with eastward propagation.

The total vorticity source (the sum of all the terms on the right hand side of Equation 1) in Figure 5b matches the vorticity tendency of Figure 5a closely. The difference (vorticity tendency minus total vorticity source; Figure 5c) is small compared to both the vorticity tendency and the total vorticity source. Note that this term includes any errors in balancing the vorticity budget and contributions from sub-gridscale processes in the model component of the reanalysis product; it will be referred to as the residual/sub-gridscale term (ϵ). Hence, to a reasonable approximation, the vorticity budget is closed, and a more detailed analysis may be carried out.

4.3. *Vorticity budget: individual source terms*

The individual vorticity source terms from Equation 1 are presented in Figure 6. Each panel shows a different source term (colour shading) along with the vorticity anomaly (line contours) repeated for reference. Recalling that the only non-zero vorticity source term for a theoretical Kelvin wave is the $-fD$ vortex stretching term (Figure 2), the $-fD$ term is first examined here, for the CCKW (Figure 6e). Qualitatively, the $-fD$ vortex stretching field does lie to the east of the vorticity anomaly, leading to an eastward propagation tendency. Hence, the basic eastward propagation mechanism of the theoretical equatorial Kelvin wave does have a role to play in the eastward propagation of the CCKW.

However, the $-fD$ vortex stretching field is clearly not in perfect quadrature with the vorticity anomaly. It is situated less than a quarter cycle to the east and is therefore partially in phase. Quantitatively, the spatial correlation coefficient from Equation 21 calculated over a 20° longitude by 10° latitude box (55–95°E, 10°S–10°N) centred on the base point at 75°E, 0°N, is $r = 0.47$, and the best fit cosine waves to the vorticity anomaly field, and the $-fD$ vorticity source field, have a phase difference of $\theta = 0.17\tau$. To calculate this phase difference, first a cosine wave of the form

$$< \zeta >= A_\zeta \cos(kx - \theta_\zeta) \tag{23}$$

is fitted to the vorticity over the longitude range 55–95°E, where the $<>$ operator denotes the latitudinal mean from the equator to 10°N, minus the latitudal mean from 10°S to the equator (taking advantage of the antisymmetric nature of the anomalies about the equator in Figure 6). Then a second cosine wave, of the form

$$< S_j >= A_{S_j} \cos(kx - \theta_{S_j}) \tag{24}$$

is fitted to the relevant source term, where the wavenumber k is the same as that in Equation 23. The phase difference is then

$$\theta = \theta_{S_j} - \theta_\zeta \, . \tag{25}$$

A quarter cycle (perfect quadrature) corresponds to a phase shift of 0.25τ, hence the phase difference here lies in the range $0 < \theta < 0.25\tau$. As discussed in Section 2.3, this will slow the propagation speed, and lead to growth. Consistently, the enstrophy tendency from the $-fD$ term is positive; $\partial E/\partial t = 7.7 \times 10^{-18}$ s^{-3}.

It is also clear that the other vorticity source terms in Figure 6 are not zero. Hence, the vorticity budget, and propagation mechanism, of an actual CCKW is significantly more complex than the simple mechanism of the theoretical equatorial Kelvin wave.

The other vortex stretching term $-\zeta D$ (Figure 6d), due to the interaction of relative vorticity with divergence, is actually the largest term with a root mean square amplitude over the 55–95°E, 10°S–10°N domain of 12.4×10^{-12} s^{-2}, compared with 7.6×10^{-12} s^{-2} for the $-fD$ vortex stretching term. However, the $-\zeta D$ vortex stretching term is almost exactly in phase with the vorticity field ($\theta = 0.03\tau$, $r = 0.80$). Hence this term barely contributes to the eastward propagation of the wave, but it does lead to large growth ($\partial E/\partial t = 21.7 \times 10^{-18}$ s^{-3}). These diagnostics of the CCKW vorticity budget for each term are collected together as the blue bars in Figure 7.

The $-\beta v$ planetary vorticity advection source term (Figure 6f) also contributes to eastward propagation and growth ($\theta = 0.09\tau$) and $\partial E/\partial t = 3.9 \times 10^{-18}$ s^{-3}, but with a smaller amplitude than the two vortex stretching terms (Figure 7). This arises physically as the meridional wind anomaly is (weakly) equatorward to the east of the cyclonic vorticity anomalies (Figure 4b). This advects high magnitude planetary vorticity (of the same sign as the relative vorticity anomalies) toward the equator, leading to an eastward propagation of the vorticity structure. As the phase difference of the $-\beta v$ source is less than 0.25τ then this source term is also partially in phase with the vorticity anomaly, and consequently also leads to growth. These three terms (both vortex stretching terms, and advecton of planetary vorticity) are the only ones that contribute to both eastward propagation and growth of the CCKW.

The zonal advection (Figure 6a) and meridional advection terms (Figure 6b) are generally out of phase with the vorticity anomaly ($\theta = 0.37\tau$ and -0.44τ, respectively; Figure 7) and have high amplitudes ($RMS = 10.6 \times 10^{-12}$ and 11.5×10^{-12} s^{-2}, respectively). Hence, they contribute strongly to destroying the wave through negative enstrophy tendencies ($\partial E/\partial t = -10.5 \times 10^{-18}$ and -13.3×10^{-18} s^{-3}). In terms of phase propagation, they approximately cancel each other; the zonal advection source lies to the east of the vorticity anomaly and gives an eastward propagation tendency, while the meridional advection source lies to the west of the vorticity and gives a westward propagation tendency. However, for the meridional advection term, the overall behaviour masks a more complex regional structure (Figure 6b). The Northern Hemisphere part of the meridional advection term is roughly in quadrature with the vorticity anomaly, leading to the westward propagation tendency, while the Southern Hemisphere part is stronger and almost exactly out of phase with the vorticity anomaly, leading to the decay tendency.

The vertical advection term (Figure 6c) is also significant ($RMS = 6.5 \times 10^{-12}$ s^{-2}), and is perfectly in phase with the vorticity anomaly ($\theta = 0.00\tau$), hence it contributes efficiently to the growth of the CCKW ($\partial E/\partial t = 11.5 \times 10^{-18}$ s^{-3}), but has no effect on propagation.

Finally, we turn to the two source terms that tilt or twist horizontal vorticity into the vertical through horizontal gradients of vertical velocity. These are usually negligible for large-scale flows in the mid-latitudes, but need to be considered here. The $-\frac{\partial \omega}{\partial x}\frac{\partial v}{\partial p}$ term (Figure 6g) is very weak ($RMS = 1.8 \times 10^{-12}$ s^{-2}) and does not contribute significantly to either propagation or growth. However, the $\frac{\partial \omega}{\partial y}\frac{\partial u}{\partial p}$ term (Figure 6h) has large amplitude ($RMS = 6.9 \times 10^{-12}$ s^{-2}). It is almost out of phase with the vorticity anomaly ($\theta = 0.47\tau$) and consequently has a large negative growth contribution ($\partial E/\partial t = -10.3 \times 10^{-18}$ s^{-3}).

Hence, even though the dynamical structure of the CCKW at 850 hPa qualitatively resembles a theoretical equatorial Kelvin wave, the vorticity budget is anything but that of a theoretical Kelvin wave. There is a complex interplay between the different terms, which must arise from the detailed structure of the CCKW, and interactions between the CCKW and the basic flow on which it is developing and propagating. The net effect of all the individual source terms are combined into the total source term (Figure 5b). This has a larger amplitude than any of the individual terms ($RMS = 14.7 \times 10^{-12}$ s^{-2}; purple bar in Figure 7a), and the total source term lies to the east of the vorticity anomaly ($\theta = 0.20\tau$). Hence the source terms collectively act to lead to eastward propagation of the CCKW, and to amplify it.

For completeness, the vorticity tendency $\partial\zeta/\partial t$ and residual/sub-gridscale ϵ terms are also included in Figure 7, as the black and yellow bars, respectively. The RMS amplitude of the residual/sub-gridscale term is less than half the magnitude of the total source term, and smaller than the four leading individual source terms.

4.4. Propagation and growth mechanisms of CCKWs

The propagation and growth characteristics from each vorticity source term are summarised graphically in a "propagation–growth" polar diagram (Figure 8). The RMS amplitude is plotted as the polar coordinate, normalised by the RMS amplitude of the vorticity tendency term $\partial\zeta/\partial t$. The phase difference θ between a source term and the vorticity anomaly is plotted as the azimuthal coordinate. The diagram can be divided into four quadrants; the position of a source term within these quadrants indicates its contribution to propagation and growth. The two blue quadrants represent propagation, with westward propagation on the left and eastward propagation on the right. The two red quadrants represent growth/decay, with growth at the top and decay at the bottom.

For reference, the vorticity source for the theoretical equatorial Kelvin wave (which is a neutral, eastward propagating wave) is shown by the grey square labelled "EKW". This has a normalised amplitude of 1, and a value of $\theta = \tau/4$, located in the blue quadrant on the right, for eastward propagation. The vorticity tendency term $\partial\zeta/\partial t$ for the CCKW is almost coincident with the position of the EKW theoretical wave, with a normalised amplitude of 1 (by design), and a value of θ very close to $\tau/4$ (note this is not guaranteed, as will be seen later with the analysis on different pressure levels).

The marker for the total source S is close to the vorticity tendency term on the polar plot, implying that the effect of the residual/sub-gridscale term (the gold ϵ marker) is small. Note that points on the polar plot are additive using a vector (or complex number) representation. For example, the sum of the vector representing the total source term (from the origin to the S marker) and the vector representing the residual/sub-gridscale ϵ term should equal the vector representing the vorticity tendency $\partial\zeta/\partial t$. Visual inspection of Figure 8 confirms this. Any discrepancy is due to errors in fitting the relevant source term maps to the idealised sinusoidal curves in Equations 23 and 24.

In this section, a more detailed analysis of the larger amplitude vorticity source terms in Figure 8 is presented. Arguments are presented for the contributions to propagation and growth/decay for each term.

4.4.1. Vortex stretching of planetary vorticity $-fD$

Although, the planetary vortex stretching $-fD$ term does lie in the blue, eastward-propagating quadrant in the propagation–growth polar diagram (Figure 8), it does not lie on the $\theta = \tau/4$ horizontal axis alongside its equivalent from the theoretical Kelvin wave (the "EKW" square). As noted in Section 4.3, the phase difference between the $-fD$ vorticity source term, and the vorticity anomaly of the CCKW, is $\theta = 0.17\tau$. How does this arise? Conveniently, the $-fD$ term (along with the $-\beta v$ term) is one of the simplest terms to interpret, as it is linear (in perturbation quantities); it is simply the CCKW divergence anomaly in Figure 4b, multiplied by f which varies with latitude. So to explain the phase difference of only 0.17τ, we need to explain the phase difference between the vorticity and divergence anomalies in the CCKW.

In a theoretical Kelvin wave, the divergence field is quarter of a cycle out of phase with (to the east of; $\theta = \tau/4$) the vorticity field (Equations 5, 6; Figure 1). This is because the wind is solely composed of the zonal component, which has a separable structure in x and y (Equation 2). The vorticity here is solely due to the shear of the zonal wind ($\zeta = -\partial u/\partial y$, as the v component is identically zero) and is in phase with the zonal wind. The divergence of the theoretical Kelvin wave is due solely to the divergence of the zonal wind ($D = \partial u/\partial x$, again, as v is identically zero) and is in quadrature with the zonal wind, and therefore the vorticity field.

In the CCKW, the meridional wind anomaly, although small, is not identically zero (Figure 4b). Could a non-zero meridional wind explain the partially in-phase relationship between vorticity and divergence in the CCKW? Close examination of the CCKW wind vector and vorticity anomalies in Figure 4b suggests that the dominant contribution to the vorticity is also from its $-\partial u/\partial y$ component, with the $\partial v/\partial x$ component having a negligible amplitude, i.e., similar to the theoretical Kelvin wave. A quantitative decomposition of the vorticity field confirms this (not shown). Similarly, the main contribution to the CCKW divergence is from $\partial u/\partial x$, with $\partial v/\partial y$ having a minor effect, again consistent with a (modified) theoretical Kelvin wave. Hence, the meridional wind component does not provide the answer.

Instead, the reason lies with a fundamental change in the spatial structure of the zonal wind anomaly. We note that although the zonal wind and divergence anomalies appear to be still very close to a quarter cycle apart (Figure 4b), the vorticity anomaly is not in phase with the zonal wind anomaly. This arises from a departure of the CCKW zonal wind field from the simple and perfectly separable sinusoidal x and Gaussian y structures of the theoretical Kelvin wave (the $\cos kx$ and $e^{-\beta y^2/2c_e}$ parts of Equation 2, respectively).

First, we note that cyclonic vorticity anomalies in the Northern and Southern Hemispheres do still flank the maximum in the equatorial westerly zonal wind anomalies of the CCKW at 70°E (Figure 4b). Hence, part of the vorticity anomaly is in phase with the zonal wind anomaly, just as in a theoretical Kelvin wave.

However, to the east, the zonal wind field of the CCKW structure has a characteristic arrowhead shape (with the arrowhead pointing eastward). For example, the first negative (dashed) contour at -0.5 m s^{-1} in Figure 4b crosses the equator at 84°E, but then curves westward and poleward into both hemispheres, such that the weak westerly anomalies on the equator at 82°E are flanked by easterly anomalies off the equator. This leads to additional cyclonic vorticity anomalies that are in phase with the anomalous convergence at these longitudes. Overall, the vorticity anomaly is shifted eastward from the zonal wind anomaly, leading to a phase difference of less than a quarter cycle between vorticity and divergence (and therefore the $-fD$ source term).

The arrowhead structure is linked to there being different trapping scales for the westerly and easterly zonal wind anomalies in the CCKW. The Gaussian trapping scale in the westerly anomalies at 70°E is $y_0 = 690$ km, corresponding to a phase speed of 5.5 m s^{-1}, as discussed in Section 4.1. However, the trapping scale in the easterly anomalies at 90°E is larger ($y_0 = 1160$ km, corresponding to a phase speed of 15.4 m s^{-1}). These two structures appear to be superimposed at the longitude where the westerlies change to easterlies (approximately 82°E). At the equator, they cancel to give approximately zero wind there. However, as the easterlies, with their larger trapping scale, decay more slowly away from the equator, there are easterly anomalies flanking the near-zero wind at the equator, leading to the off-equatorial cyclonic vorticity anomalies.

Hence, the $-fD$ vortex stretching term contributes to both propagation and growth. The observed propagation speed of the CCKW is approximately 10 m s^{-1}, which is the average of the two modal propagation speeds diagnosed from the westerly and easterly anomalies (5 and 15 m s^{-1}). The reason for these two spatial structures is not clear, and the issue is discussed in the conclusions (Section 6).

4.4.2. Vortex stretching of relative vorticity $-\zeta D$

An analysis of the second vortex stretching term, that due to the relative vorticity, now follows. The $-\zeta D$ term lies clearly in the growth quadrant of the propagation–growth polar diagram

(Figure 8). This source term is non-linear, as it is the product of two spatio-temporally varying quantities. Hence, there may be a role for interactions between the dynamical fields of the CCKW and the "basic state" or background flow, that the CCKW propagates and develops on. Any quantity, e.g., relative vorticity, can be decomposed into contributions from the basic state and the perturbation:

$$\zeta = \overline{\zeta} + \zeta' \,, \tag{26}$$

where the overbar denotes the basic state, and the prime denotes the perturbation. Here, the perturbation is defined as the CCKW-filtered anomaly, and the basic state is the remainder (total minus perturbation field). Hence the non-linear vorticity source term here can be decomposed into interactions between the basic state and the perturbation:

$$-\,\zeta D = -\overline{\zeta}\,\overline{D} - \overline{\zeta}D' - \zeta'\overline{D} - \zeta' D' \,. \tag{27}$$

Each of the four terms in Equation 27 can then be wavenumber–frequency filtered and lag-composited to extract the CCKW signal, as previously. The CCKW composite of the first term ($-\overline{\zeta}\,\overline{D}$) is essentially zero, by design. The remaining three terms can then be compared with the full $-\zeta D$ term, shown previously in Figure 6d.

The major contribution is from $-\overline{\zeta}D'$ (Figure 9a), which is the effect of the divergence perturbation from the CCKW spinning up the basic state vorticity. For the basic state vorticity, rather than using a mean background vorticity calculated over the entire 1998–2018 study period, a mean background vorticity specific to these CCKWs is calculated, by compositing the background vorticity ($\overline{\zeta}$) over the 122 days at which the CCKWs crossed the basepoint longitude of 75°E. This background flow is then spatially smoothed by spectral truncation at total wavenumber 42 (Figure 10). In anticipation of the analysis of further source terms, the background 850-hPa vector wind and divergence fields were also calculated in Figure 10. The CCKW events had a slight seasonal bias, with 60% being in the northern summer (May–October) season, and 40% in the northern winter (November–April) season.

The mean background flow in Figure 10 is consistent with this, showing the flow associated with the Asian summer monsoon, with northeastward flow in the Southern Hemisphere, northward flow across the equator over the western Indian Ocean, and then a southeastward flow in the Northern Hemisphere over the Arabian Sea to around 80°E, which then curves to the northeast over the Bay of Bengal. Associated with this background flow, the background vorticity is cyclonic in the Southern Hemisphere (negative anomalies from 0–10°S in Figure 10) with a peak near 80°E, and also cyclonic in the Northern Hemisphere around Sri Lanka (positive anomalies).

The $-\overline{\zeta}D'$ vorticity source term in Figure 9a is then consistent with the D' divergence anomaly from the CCKW in Figure 4b spinning up the background vorticity in Figure 10. In particular, the negative D' anomaly (convergence) in Figure 4b extends further from the equator into the Southern Hemisphere than into the Northern Hemisphere, and the cyclonic $\overline{\zeta}$ structure in the Southern Hemisphere overlaps this convergence more than its counterpart in the Northern Hemisphere (the zero line of $\overline{\zeta}$ in Figure 10 is at 2°N rather than exactly on the equator. Both of these subtle differences lead to the $\overline{\zeta}D'$ term in Figure 9a being much stronger in the Southern Hemisphere than in the Northern Hemisphere. The resulting $-\overline{\zeta}D'$ source term in the Southern Hemisphere is such then almost in phase with the CCKW vorticity anomaly (line contours in Figure 9a), leading to this term contributing strongly to the growth of the CCKW.

There is a smaller contribution from $-\zeta'\overline{D}$ (Figure 9b), which represents the interaction of the basic state divergence with the perturbation vorticity from the CCKW. The background divergence field (line contours in Figure 10) shows convergence (negative $\overline{D}$) throughout the tropical Indian Ocean, that is fairly spatially uniform in the equatorial belt. Hence, the resulting $-\zeta'\overline{D}$ source term is approximately a constant multiplier of the CCKW ζ' vorticity field, and is therefore almost perfectly in phase with it (Figure 9b), again leading to growth of the CCKW.

The contribution from $-\zeta' D'$ (the interaction between the perturbation vorticity and divergence fields) is negligible (not shown). An explanation of the relative magnitudes of the previous two terms can be gained from a scale analysis of the relevant fields. From Figure 10, $|\overline{\zeta}| \sim 10 \times 10^{-6}$ s^{-1}, and $|\overline{D}| \sim 1 \times 10^{-6}$ s^{-1}. From Figure 4b, $|\zeta'| \sim 3 \times 10^{-6}$ s^{-1}, and $|D'| \sim 1.5 \times 10^{-6}$ s^{-1}. Hence, $|-\overline{\zeta}D'| \gg |-\zeta'\overline{D}|$, consistent with the fields in Figure 9a,b. However, from this scale analysis, we might also expect that the $-\zeta' D'$ term be of similar magnitude to the $-\zeta'\overline{D}$ term.

The reason for the negligible magnitude of the $-\zeta' D'$ term can be understood from a consideration of the interaction between two sinosoidal waves. First, we allow a theoretical equatorial Kelvin wave to have finite amplitude. Hence, the non-linear $-\zeta' D'$ term is not immediately discounted in the vorticity equation due to its amplitude being the product of two infinitessimal perturbation terms, and therefore negligible compared to the linear terms. However, the $-\zeta' D'$ term in the theoretical wave would still be zero, as the divergence field is quarter of a cycle out of phase with the vorticity field, as discussed in Section 4.4.1 for the $-fD$ term. Because of this quadrature relationship, the product $-\zeta' D'$, when spatially averaged, would then be zero.

Moving on from the theoretical Kelvin wave to the observed CCKW, we note that the phase shift between the vorticity ζ' and divergence D' fields is not exactly a quarter cycle. However, it transpires that the the growth from the $-\zeta' D'$ source term (or indeed any of the nonlinear perturbation source terms) will tend to be zero, whatever the phase shift between the fields. For example, if the longitudinal dependence of the vorticity structure does vary as a sinusoid $\zeta' = \cos(kx)$, and the divergence structure has a similar structure with the same wavenumber, but phase shifted as $D' = \cos(kx - \phi)$, then the source term is

$$-\,\zeta' D' = -\frac{1}{2}\left[\cos(2kx - \phi) + \cos\phi\right] \,. \tag{28}$$

This has the form of a wave with double the wavenumber of the constituent vorticity and divergence fields, and a constant term. The mean value of the source term is the constant $-\frac{1}{2}\cos\phi$. However, the enstrophy generation (Equation 20) calculated from these pure sine wave structures will be proportional to the integral (over an integer number of wavelengths) of

$$\int \zeta' \left(-\zeta' D'\right) dx = -\int \cos^2(kx)\, \cos(kx - \phi)\, dx = 0, \tag{29}$$

which is identically zero, whatever the value of the phase shift ϕ between the vorticity and divergence fields. Although the observed CCKW vorticity and divergence fields are not exactly pure sinusoids in the zonal direction, the majority of their structure is modelled by a pure sinusoidal wave, and hence the integrated growth from the $-\zeta' D'$ term will be small.

In summary, the $-\overline{\zeta}D'$ term leads to growth and eastward propagation, the $-\zeta'\overline{D}$ term leads to growth, and the $-\zeta' D'$ term is negligible.

4.4.3. *Zonal advection* $-u\,\partial\zeta/\partial x$

The zonal advection term lies on the boundary between eastward propagation and decay in the propagation–growth polar diagram (Figure 8), and therefore has an equal contribution to both. This non-linear term can also be decomposed into interactions between the basic state and the perturbation. The dominant and only non-negligible contribution is from the $-\overline{u}\,\partial\zeta'/\partial x$ term (Figure 9c). This is advection of the perturbation vorticity structure in Figure 4 by the background flow at this level.

The strongest background zonal flow $\overline{u}$ (Figure 10), in the latitude band 10°S–10°N, where the vorticity anomalies in Figure 4 are large, is the eastward flow over the Northern Hemisphere Indian Ocean. This is consistent with the largest values for the zonal advection $-u\,\partial\zeta/\partial x$ (Figure 6a), and $-\overline{u}\,\partial\zeta'/\partial x$ (Figure 9c) terms also being in the Northern Hemisphere. These eastward winds lead to the $-\overline{u}\,\partial\zeta'/\partial x$ source terms being to the east of the vorticity perturbations, and therefore to eastward propagation.

The zonal advection term is weaker in the Southern Hemisphere, but is still consistent with advection by the background flow. The background zonal winds in the Southern Hemisphere, in the 0–10°S band, where the perturbation vorticity anomalies are strongest, are weak westward winds in the southern half of this domain and actually switch to eastward winds at around 3°S, i.e., before the equator. Hence, over the whole equatorial belt, the background zonal winds are eastward, leading to eastward advection and aiding the eastward propagation of the CCKWs.

In addition to aiding eastward propagation, the zonal advection term also has a negative growth contribution for the CCKW (Figure 8). This is initially surprising, as the vorticity source terms (colour shading in Figure 9c) appear to be in quadrature with the vorticity anomalies (line contours in Figure 9c). However, close examination shows that, e.g., the negative $-\overline{u}\,\partial\zeta'/\partial x$ anomalies centred at approximately 6°N, 65°E have a larger spatial extent than the positive $-\overline{u}\,\partial\zeta'/\partial x$ anomalies centred at approximately 6°N, 85°E. Both these source terms overlap with the positive vorticity anomaly, hence the net result is a negative vorticity tendency in a region of positive vorticty anomaly, leading to decay. This result is due to the CCKW not having a perfect, repeating sinusoidal structure like the theoretical equatorial Kelvin wave, and also due to a non-constant background zonal wind, as discussed below.

This contribution to growth/decay may appear surprising, as advection is inherently a propagation rather than a growth process. However, this can be explained by considering the enstrophy generation (Equation 20) due to zonal advection,

$$\frac{\partial E}{\partial t} = \frac{2}{R}\iint_R \zeta' \left(-\overline{u}\frac{\partial \zeta'}{\partial x}\right) dx\,dy = -\frac{1}{R}\iint_R \overline{u}\frac{\partial}{\partial x}\left(\zeta'^2\right) dx\,dy\,. \tag{30}$$

integrating by parts gives

$$\frac{\partial E}{\partial t} = -\frac{1}{R}\left[\overline{u}\left(\zeta'^2\right)\right] + \frac{1}{R}\iint_R \left(\zeta'^2\right)\frac{\partial \overline{u}}{\partial x}\,dx\,dy. \tag{31}$$

The first term on the right hand side will be zero if the domain R extends beyond the perturbation. If the background wind is constant, then $\partial\overline{u}/\partial x = 0$, the second term on the right hand side is also zero, and there is no enstrophy generation and no growth. However, if the background wind is not constant, there can be growth. From Equation 31, divergence (convergence) of the background wind leads to an increase (decrease) in enstrophy and growth (decay).

Furthermore, the zonal advection of perturbation vorticity by the background wind, and the vortex stretching by the perturbation vorticity acting on the background zonal divergence, can be combined together in flux form,

$$-\,\overline{u}\frac{\partial\zeta'}{\partial x} - \zeta'\frac{\partial\overline{u}}{\partial x} = -\frac{\partial}{\partial x}(\overline{u}\zeta')\,. \tag{32}$$

For typical distributions, these two terms tend to partially cancel, further compounding the analysis.

4.4.4. *Meridional advection $-v\,\partial\zeta/\partial y$*

The meridional advection term contributes to decay in the propagation–growth polar diagram (Figure 8). Examination of the $-v\partial\zeta/\partial y$ vorticity source term (Figure 6b) shows this is mainly due to the overlap of the positive vorticity source with the negative vorticity anomaly, south of the equator between 65 and 80°E. Decomposition reveals that this is almost entirely due to the $-\overline{v}\partial\zeta'/\partial y$ term (advection of perturbation vorticity by the background meridional wind; Figure 9d).

The background meridional wind is predominantly northward over the equatorial Indian Ocean (Figure 10). Consistent with this, in the 65–85°E band (the core of the CCKW considered in this study), there is a negative $-\overline{v}\partial\zeta'/\partial y$ source term to the north of the negative vorticity anomaly in the Southern Hemisphere, and a positive source term to its south. This is consistent with northward advection, as would be expected from a northward wind. This northward advection of the CCKW will then have a tendency to displace the CCKW northward of its usual eastward trajectory along the equator.

However, our main consideration here is the effect of the meridional advection term on the growth and decay of the CCKW. The strength of the background northward wind $\overline{v}$ is not constant, with it decreasing toward the north in the core CCKW region. Hence, in the Southern Hemisphere, the positive advective tendency to the south of the vorticity minimum at 3°S, is stronger than the negative tendency to the north of the vorticity minimum (Figure 9d). In the Northern Hemisphere, there is a strong negative tendency to the south of the vorticity maximum at 6°N, but only a very weak tendency to the north of this maximum. Hence, when integrated over the CCKW domain, the meridional advection tendency destructively interferes with the CCKW vorticity field and leads to decay.

5. Vertical structure of CCKWs

To elicit any variations of the propagation and growth mechanisms of CCKWs in the vertical, the CCKW composite structure and vorticity budget has been calculcated at three further pressure levels.

5.1. *Boundary layer: 975 hPa*

The 850 hPa level in Section 4 was chosen to present the vorticity budget at the standard level in the free lower troposphere. Here, any effects of the boundary layer are investigated by a similar analysis at the 975 hPa level. The zero-lagged CCKW structure in the boundary layer at 975 hPa (Figure 11c) is very similar to that at 850 hPa just above (Figure 4b). The structure at 975 hPa is shifted eastward, relative to 850 hPa. This is consistent with the well-known westward tilt with height of the CCKW structure (Wheeler et al. 2000).

One process of potential interest in the boundary layer is frictional convergence. Here, the easterly wind anomalies to the east of the precipitation anomaly at the base point might be expected to develop an equatorward component (i.e., northerly in the Northern Hemisphere, and southerly in the Southern Hemisphere) toward the low pressure centre at the equator (not shown), once the frictional force in the boundary layer is added to the horizontal force balance between the pressure gradient and Coriolis forces. This mechanism has previously been proposed to help explain the eastward propagation of the MJO through its effect on converging moisture ahead (to the east) of the convective anomaly (Maloney and Hartmann 1998). Any effect on the moisture budget of the CCKWs is beyond the scope of the dry dynamical vorticity budget analysed here, but a change in the meridional wind component and its effect on divergence could affect the vortex stretching ($-\zeta D$ and $-fD$) and advection of planetary vorticity ($-\beta v$) terms.

Close examination of the velocity structure in Figure 11c reveals that there is an equatorward component of the flow (and hence a frictional convergence contribution) to the east of the precipitation anomaly, but it is weak. The individual vorticity source terms at all levels are summarised in a propagation–growth polar diagram (Figure 12). The 850-hPa terms are indicated by circular markers as before, and the 975, 500 and 200-hPa terms are indicated by upward pointing triangles, stars, and downward pointing triangles, respectively. The markers at each level are joined by lines, creating a "constellation" pattern for each vorticity source term.

As anticipated, the two vortex stretching terms ($-\zeta D$ and $-fD$) and advection of planetary vorticity ($-\beta v$) at 975 hPa in the boundary layer do have higher (relative) amplitudes than their counterparts at 850 hPa. Additionally, the $-\beta v$ term at 975 hPa contributes exclusively to eastward propagation, due to the equatorward advection of cyclonic vorticity to the east of the existing cyclonic vorticity structures. However, these changes are small.

Vertical advection ($-\omega\partial\zeta/\partial p$) and the two tilting/twisting terms have even smaller amplitudes at 975 hPa compared with 850 hPa, as might be expected due to the proximity to the surface and associated suppresion of vertical velocities.

Overall, there is little qualitative difference between the vorticity budgets at 975 and 850 hPa. The conclusion is that, perhaps surprisingly, the boundary layer does not have a significant dynamical effect on the propagation and growth mechanisms of CCKWs.

5.2. *Middle troposphere: 500 hPa*

In this section, the mid-tropospheric structure and vorticity budget is examined. The 500 hPa level is chosen, which has been previously identified as a level of large CCKW amplitude (Wheeler et al. 2000; Yang et al. 2007a). The vertical structure of the CCKW again shows the well-known westward tilt with height, such that at 500 hPa, the westerly wind anomalies now peak at 57°E, and the easterly anomalies peak near 80°E (Figure 11b), directly above the convergence at 850 hPa (Figure 4b).

The dynamical structure at 500 hPa shows an even stronger deviation from a single mode structure, than it did at 850 hPa, as the (negative) zonal wind anomalies extend diagonally polewards and westwards into both hemispheres (like an arrowhead pointing eastward, in the direction of propagation), rather than just decaying polewards with a simple, single Gaussian structure. This is reminiscent of the dynamical structures observed in mixed Rossby–gravity waves (Kiladis et al. 2016), westward-propagating inertio-gravity waves (Takayabu 1994; Tulich and Kiladis 2012), and the MJO (Adames and Wallace 2014). The zonal wind anomalies at 500 hPa also clearly extend further from the equator than they do at 850 hPa.

This behaviour can be approximately modelled by the superposition of two modes, with different latitudinal trapping scales y_1 and y_2, and different longitudinal phase shifts ϕ_1 and ϕ_2. Hence, the zonal wind field from the zero-lag composite at 500 hPa in Figure 11b was subjected to a least-squares fit to the function

$$u(x,y) = u_0 \left[\alpha e^{-(y/y_1)^2} \cos(kx - \phi_1) + (1-\alpha)e^{-(y/y_2)^2} \cos(kx - \phi_2)\right], \tag{33}$$

over the domain 50–100°E, 15°S–15°N. Here, the value of u_0 was constrained to be the largest magnitude value observed in the domain (-2.3 m s^{-1}), and y_1 was constrained to be the same value as diagnosed for the single mode at 850 hPa (690 km, corresponding to a theoretical phase speed of $c_1 = 5.5$ m s^{-1}).

The best-fit values of the free parameters gave a Gaussian trapping scale of $y_2 = 1,890$ km for the second mode, corresponding to a theoretical Kelvin wave phase speed of $c_2 = 41$ m s^{-1}, a partition between the first and second mode of $\alpha = 0.67$, a wavenumber of $k = 0.87 \times 10^{-6}$ m^{-1}, and a relative phase shift between the two modes of $\phi_1 - \phi_2 = 0.20\tau$, i.e., a fifth of a wavelength. Hence, it appears that although the basic theoretical Gaussian structure is still a realistic model for the observed CCKW in the lower troposphere, dynamical mechanisms in the mid-troposphere have distorted the CCKW structure significantly away from a theoretical single-mode Kelvin wave. This is discussed further in Section 6.

The terms in the vorticity budget are shown by the star markers in the constellation plot of Figure 12. Unlike at the other levels, the vorticity tendency does not show pure eastward propagation at this level; it also indicates growth. The total source term is very close by in the polar plot, consistent with the very small amplitude residual/sub-gridscale ϵ term, and a high degree of closure of the vorticity budget.

The main sources of growth at 500 hPa are from the two vortex stretching terms ($-\zeta D$ and $-fD$). Both these terms contribute, albeit weakly, to eastward propagation also. However, their impact is strongly negated by the two horizontal advection terms, both of which have a negative growth tendency, and (weak) westward propagation. Vertical advection has a (weak) eastward propagation contribution. Both the $-\beta v$ and the first tilting ($-\partial\omega/\partial x\, \partial v/\partial p$) terms are very weak. The second tilting term ($\partial\omega/\partial y\, \partial u/\partial p$) contributes weakly to decay and eastward propagation. Overall, the CCKW structure and its vorticity budget in the middle troposphere is more complex than in the lower troposphere.

5.3. *Upper troposphere: 200 hPa*

The lower and middle tropospheric layers previously examined are characterised by convergent inflow into the region of CCKW enhanced precipitation (Figures 4b, 11b,c here; Wheeler et al. 2000), albeit with a westward tilt with height. The 200 hPa level is representative of divergent outflow in the upper troposphere. Consistent with this, there is a region of anomalous divergence in the CCKW structure (Figure 11a) located within and to the west of the precipitation maximum (Figure 3b).

However, the basic dynamical CCKW structure at this level is very different from that in the lower and middle troposphere, as previously reported by Yang et al. (2007c). The meridional wind component is as large as the zonal wind component; hence the CCKW at this level cannot just be considered as a modified equatorial Kelvin wave. This meridional wind represents divergent outflow and extends poleward to 20° latitude in both hemispheres. It can be considered as a local Hadley circulation response to the CCKW ascending motion within the precipitation anomaly.

Not surprisingly, the vorticity budget of the CCKW at 200 hPa (downward pointing triangles in Figure 12) is also not consistent with a modified equatorial Kelvin wave. The vorticity tendency is consistent with eastward propagation as with the lower levels, as it must be because the whole CCKW structure does propagate eastward as a coherent entity. However, the individual vorticity source terms that contribute to this are very different. The $-fD$ vortex stretching term, the main agent of eastward propagation for the CCKW at lower levels and the sole agent for the theoretical Kelvin wave, has no contribution to propagation at 200 hPa, and actually leads to decay of the wave. This arises from the positive divergence anomalies being alongside the cyclonic vorticity anomalies (Figure 11a) rather than to the west of them.

The cyclonic vorticity anomalies themselves arise as much from the meridional wind as from the zonal wind anomalies. The $-\zeta D$ vortex stretching term is an agent for growth and (weak) westward propagation, and is strongly controlled by interactions with the basic state.

Zonal and meridional advection lead to strong westward propagation/growth and growth/eastward propagation, respectively. Again, both source terms contain strong interactions with the basic state. Vertical advection leads to growth. The strong meridional wind anomalies at 200 hPa give rise to strong meridional advection of planetary vorticity ($-\beta v$), which is an agent for westward propagation (via the *Rossby* wave mechanism) and decay. The first and second tilting terms are weak and lead to strong eastward propagation, respectively.

Hence, in the upper troposphere, there is not a Kelvin wave mechanism operating at all. The overall combination of source terms with cancelling growth and decay contributions, and tendencies for both westward and eastward propagation, combine in a complex way to a net eastward propagation, with some decay. An interpretation of this is that the (convectively coupled) equatorial Kelvin wave mechanism operates strongly in the lower troposphere, where the moisture source that ultimately powers the CCKW and the convective triggers that organise it are located, while the upper tropospheric component arises as a forced response to this, that must follow the eastward-propagating lower tropospheric component.

6. Conclusions

The dynamical propagation and growth mechanisms of CCKWs over the Indian Ocean have been investigated using a vorticity budget approach. A modified equatorial Kelvin wave mechanism operates in the lower troposphere.

The $-fD$ vortex stretching term contributes most to the eastward propagation of the CCKW, as in a theoretical Kelvin wave. It also contributes to growth, through the deviation of the zonal wind and resulting vorticity distributions from a theoretical single mode structure. The westerly wind anomalies in the CCKW have a trapping scale of 690 km, with a corresponding theoretical phase speed of 5.5 m s^{-1}, but the easterly wind anomalies have a larger trapping scale of 1160 km, corresponding to a phase speed of 15.4 m s^{-1}. Hence, in the lower troposphere, it appears that two distinct Kelvin wave modes are in operation. Eastward propagation of the CCKW is also aided by advection by the background lower tropospheric westerly flow over the Indian Ocean. The results here emphasise the importance of the background flow in the lower troposphere in aiding eastward propagation, in contrast to Dias and Kiladis (2014), who found no universal steering level, but concluded that the westerly barotropic component of the background winds was more instrumental in leading to faster eastward propagation of CCKWs.

The main growth contribution is from the $-\zeta D$ vortex stretching term, mainly due to a belt of background cyclonic vorticity in the Southern Hemisphere Indian Ocean, that spins up the CCKW divergence field as it transits through. This is partially countered by decay from the zonal and meridional vorticity advection terms, with the dominant contribution being advection of the perturbation (CCKW) vorticity by the background winds. The other vorticity source terms have a relatively small contribution to CCKW growth and propagation over the Indian Ocean. Hence, this analysis suggests a simplified vorticity equation for CCKWs over the Indian Ocean,

$$\frac{\partial \zeta'}{\partial t} \approx \underset{\substack{\text{eastward}\\ \text{decay}}}{-\bar{u}\frac{\partial \zeta'}{\partial x}} \quad \underset{\text{decay}}{-\bar{v}\frac{\partial \zeta'}{\partial y}} \quad \underset{\text{growth}}{-\bar{\zeta}D'} \quad \underset{\substack{\text{eastward}\\ \text{growth}}}{-fD'}\,. \qquad (34)$$

In the middle troposphere, the CCKW shows its well known westward tilt with height. Additionally, the horizontal structure is more complex, with a two-mode structure being more prevalent. The middle tropospheric westerly wind anomalies have a similar trapping scale to the lower tropospheric structure, but the easterly anomalies have a much larger trapping scale of 1890 km, corresponding to a phase speed of 41 m s^{-1}.

The trapping scale of a Kelvin wave mode is linked to its phase speed through Equation 4, and to an equivalent depth h_n through $c_e^2 = gh_n$. The equivalent depth arises from the separation constant when the full primitive equations are separated into the shallow water equations governing the x, y, t behaviour, of which the Kelvin wave in Equation 2 is a solution, and the vertical structure equation, which governs the p behaviour and leads to distinct vertical modes.

These vertical modes are excited by the vertical structure of the embedded convective heating. In an analysis of mean tropical atmospheric conditions, Haertel and Kiladis (2004) found values for the phase speeds of 49 m s^{-1} for the first internal mode (forced by deep convective heating of same sign throughout troposphere, peaking at mid levels), and 23 m s^{-1} for the second internal mode, forced by heating of opposite sign in the lower and upper troposphere. Both these vertical modes have previously been found to be important for CCKWs (Straub and Kiladis 2003). More complex heating structures with more sign changes in the vertical will correspond to smaller equivalent depths and phase speeds. The range of trapping scales (and phase speeds) diagnosed here in the CCKW structure are qualitatively consistent with those of the first few baroclinic modes of the tropical atmosphere.

Convection in CCKWs (along with other convectively coupled equatorial waves, and the MJO) passes through a life cycle of different cloud populations with different vertical heating structures, from shallow convection to deep convection (Tulich and Mapes 2008; Kiladis et al. 2009). Hence, the aggregated structure will be a combination of a forced and free response to the spatio-temporally varying convective heating.

The CCKW structure and vorticity balance in the upper troposphere are not those of an equatorial Kelvin wave at all, containing a strong local Hadley-like circulation. The upper tropospheric CCKW structure is interpreted as a dynamical adjustment to the forcing in the lower troposphere.

It should be restated that the analysis here, using the vorticity equation, is a purely dry dynamical approach. The vorticity budget is valid on its own at each level, but it is clear that the production of CCKWs depends on the strength and nature of the interaction between moist convection and dynamics (e.g., Peatman et al. 2018). Hence, to fully understand the vertical structure and the interplay between the different levels, it will be necessary to mesh this approach with a similar analysis of the thermodynamical and moisture budgets. This will be attempted in a future study.

It could be argued that this may have been partially accomplished by calculating a potential vorticity budget rather than a vorticity budget, as potential vorticity contains both dynamical and thermodynamical information. However, (shallow water) potential vorticity for a theoretical equatorial Kelvin wave is identically zero as the dynamical and thermodynamical contributions exactly cancel. Nevertheless, potential vorticity is available as a pre-calculated output for some reanalyses, e.g., ERA-Interim, and a future study could investigate the partitioning of potential vorticity between the dynamical and thermodynamical contributions in observed CCKWs.

Preliminary analysis indicates that the mass (geopotential) field of the composite CCKW structure is shifted westward relative to the zonal wind field consistent with Roundy (2012), rather than being in phase with it as in the theoretical linear equatorial Kelvin wave. As the mass field is linked to the temperature field and diabatic heating through hydrostatic balance, this phase shift shows that that diabatic thermodynamical and moist convective processes have a first order impact on the CCKW structure.

The approach developed here can be expanded on and applied to other situations to answer further questions. In this study, the Indian Ocean was chosen as climatologicaly it contains the largest number of CCKWs. Do CCKWs in other regions, such as the Pacific Ocean with its easterly background wind field, obey the same vorticity balance as CCKWs in the Indian Ocean? Is there a seasonal dependence to the CCKW vorticity balance? The phase of the MJO is known to modulate the amplitude and frequency of CCKW events (Roundy 2008; Baranowski et al. 2016a). Does the phase of the MJO also affect the internal CCKW vorticity balance?

Individual CCKW events pass through a life cycle (Kiladis et al. 2009). Here, the CCKW vorticity budget was calculated with respect to the crossing time at a fixed longitude, irrespective of the stage of each event within its own life cycle. An alternative vorticity budget could be carried out based on the position of events within their life cycles, to determine whether key processes are important at different times in the life cycle.

The vorticity budget approach presented here can be applied to output from climate model simulations. Previous work on the simulation of CCKWs in climate models has highlighted the importance of the convective parameterisation scheme. For models in the Coupled Model Intercomparison Project 3 generation (CMIP3), the inclusion of a trigger (Straub et al. 2010) or convective suppression (Huang et al. 2013) led to relatively successful simulations of CCKWs in terms of overall amplitude and global distribution. In the later CMIP5 generation, most models correctly simulated the CCKW phase propagation over the Indian Ocean, but underestimated its speed over the Pacific sector (Yang and Li 2016). However, a dynamical CCKW budget akin to the one presented here does not appear to have been carried out on CMIP models. The results of such an analysis should help elucidate the origins of the systematic errors in those models.

CCKWs have been analysed in numerical weather predictions (NWP) and are generally too weak (Dias et al. 2018; Janiga et al. 2018). Phase speeds can be either too fast (Dias et al. 2018; Yang et al. 2021) or too slow (Janiga et al. 2018). Again, a dynamical vorticity budget analysis could be applied to NWP output to help further diagnose these systematic errors.

Finally, the vorticity budget approach can be adapted to diagnose propagation and growth mechanisms in other types of convectively coupled equatorial waves, such as equatorial Rossby waves, and mixed Rossby-gravity waves.

Acknowledgement

The ERA-Interim data were provided by the Centre for Environmental Data Analysis. The 3B42 data were provided by the NASA/Goddard Space Flight Center and PPS, which develop and compute the 3B42 dataset as a contribution to the TRMM project, and archived at the NASA GES DISC. The research presented in this paper was carried out on the High Performance Computing Cluster supported by the Research Computing Service at the University of East Anglia. AJM was partially funded by the Natural Environment Research Council through the Equatorial Line Observations (ELO) project (grant NE/R012431/1) and the TerraMaris project (grant NE/R016704/1). I thank George Kiladis and an anonymous reviewer for comments that helped to significantly improve the manuscript.

References

Abbott S. 2012. My conversion to tauism. *Math Horizons,* **19,** 34, doi: 10.4169/mathhorizons.19.4.34.

Adames AF, Wallace JM. 2014. Three-dimensional structure and evolution of the MJO and its relation to the mean flow. *J. Atmos. Sci.,* **71,** 2007–2026, doi: 10.1175/JAS-D-13-0254.1.

Baranowski DB, Flatau MK, Flatau PJ, Matthews AJ. 2016a. Impact of atmospheric convectively-coupled Kelvin waves on upper ocean variability. *J. Geophys. Res.,* **121,** 2045–2059, doi: 10.1002/2015JD024150.

Baranowski DB, Flatau MK, Flatau PJ, Matthews AJ. 2016b. Phase locking between atmospheric convectively coupled equatorial Kelvin waves and the diurnal cycle of precipitation over the Maritime Continent. *Geophys. Res. Lett.,* **43,** 8269–8276, doi: 10.1002/2016GL069602.

Baranowski DB, Flatau MK, Flatau PJ, Schmidt JM. 2017. Multiple and spin off initiation of atmospheric convectively coupled Kelvin waves. *Climate Dyn.,* **49,** 2991–3009, doi: 10.1007/s00382-016-3487-7.

Baranowski DB, Flatau MK, Flatau PJ, Karnawati D, Barabasz K, Labuz M, Latos B, Schmidt JM, Paski JAI, Marzuki. 2020. Social-media and newspaper reports reveal large-scale meteorological drivers of floods on Sumatra. *Nature Communicat.,* **11,** 2503 , doi: 10.1038/s41467-020-16171-2.

Blaauw M, Zagar N, 2018: Multivariate analysis of Kelvin wave seasonal variability in ECMWF L91 analyses. Atmos. Chem. Phys., 18, 8313-8330, doi: 10.5194/acp-18-8313-2018.

Dawson A. 2016. Windspharm: A high-level library for global wind field computations using spherical harmonics. *J. Open. Res. Soft.,* **4,** e31, doi: 10.5334/jors.129.

Dee DP, Uppala SM, Simmons AJ, Berrisford P, Poli P, Kobayashi S, Andrae U, Balmaseda MA, Balsamo G, Bauer P, Bechtold P, Beljaars ACM, van der Berg L, Bidlot J, Bormann N, Delsol C, Dragani R, Fuentes M, Geer AJ, Haimberger L, Healy SB, Hersbach H, Holm EV, Isaksen L, Kallberg P, Kohler M, Matricardi M, McNally AP, Monge-Sanz BM, Morcrette J-J, Park B-K, Peubey C, de Rosnay P, Tavolato C, Thepaut J-N, Vitart F. 2011. The ERA-Interim reanalysis: configuration and performance of the data assimilation system. *Quart. J. Roy. Meteorol. Soc.,* **137,** 553–597, doi: 10.1002/qj.828.

Dias J, Kiladis GN, 2014. Influence of the basic state zonal flow on convectively coupled equatorial waves. *Geophys. Res. Lett.,* **41,** 6904–6913, doi: 10.1002/2014GL061476.

Dias J, Gehne M, Kiladis GN, Sakaeda N, Bechtold P, Haiden T, 2018. Equatorial waves and the skill of NCEP and ECMWF numerical weather prediction system. *Mon. Weath. Rev.,* **146,** 1763–1784, doi: 10.1175/MWR-D-17-0362.1.

Dunkerton TJ, Crum FX, 1995. Eastward propagating 2 to 15-day equatorial convection and its relation to the tropical intraseasonal oscillation. *J. Geophys. Res.,* **100,** 25871–25790, doi: 10.1029/95JD02678.

Ferrett S, Yang G-Y, Woolnough S, Methven J, Hodges K, Holloway CE. 2020. Linking extreme precipitation in southeast Asia to equatorial waves. *Quart. J. Roy. Meteorol. Soc.,* **146,** 665–684, doi: 10.1002/qj.3699.

Gehne M, Kleeman R, 2021: Spectral analysis of tropical atmospheric dynamical variables using a linear shallow-water modal decomposition. *J. Atmos. Sci.,* **69,** 2300–2316, doi: 10.1175/JAS-D-10-05008.1.

Gill AE. 1980. Some simple solutions for heat-induced tropical circulation. *Quart. J. Roy. Meteorol. Soc.,* **106,** 447–462, doi: 10.1002/qj.49710644905.

Gill AE. 1982. Atmosphere–ocean dynamics. *Academic Press,* 662 pp.

Guo Y, Jiang X, Waliser DE. 2014. Modulation of the convectively coupled Kelvin waves over South America and the tropical Atlantic Ocean in association with the Madden-Julian Oscillation. *J. Atmos. Sci.,* **71,** 1371–1388, doi: 10.1175/JAS-D-13-0215.1.

Guo Y, Waliser DE, Jiang X. 2015. A systematic relationship between the representations of convectively coupled equatorial wave activity and the Madden-Julian Oscillation in climate model simulations. *J. Climate,* **28,** 1881–1904, doi: 10.1175/JCLI-D-14-00485.1.

Haertel PT, Straub KH, Budsock A. 2015. Transforming circumnavigating Kelvin waves that initiate and dissipate the Madden–Julian oscillation. *Quart. J. Roy. Meteorol. Soc.,* **141,** 1586–1602, doi: 10.1002/qj.2461.

Haertel PT, Kiladis GN, 2004. Dynamics of 2-day equatorial waves. *J. Atmos. Sci.,* **61,** 2707–2721, doi: 10.1175/JAS3352.1.

Huffman GJ, Adler RF, Bolvin DT, Gu GJ, Nelkin EJ, Bowman KP, Hoong Y, Stocker EF, Wolff DB. 2007. The TRMM multisatellite precipitation analysis (TMPA): Quasi-global, multiyear, combined-sensor precipitation estimates at fine scales. *J. Hydrometeorol.,* **8,** 38–55, doi: 10.1175/JHM560.1.

Huang P, Chou C, Huang R, 2013. The activity of convectively coupled equatorial waves in CMIP3 global climate models. *Theoret. Appl. Climatol.,* **112,** 697–711, doi: 10.1007/s00704-012-0761-4.

Janiga MA, Schreck JC, Ridout JA, Flatau M, Barton NP, Metzger EJ, Reynolds CA, 2018. Subseasonal forecasts of convectively coupled equatorial waves and the MJO: Activity and predictive skill. *Mon. Weath. Rev.,* **146,** 2337–2360, doi: 10.1175/MWR-D-17-0261.1.

Kikuchi K, 2014. An introduction to combined Fourier-wavelet transform and its application to convectively coupled equatorial waves. *Clim. Dyn.,* **43,** 1339–1356, doi: 10.1007/s00382-013-1949-8.

Kikuchi K, Kiladis GN, Dias J, Nasuno T, 2018. Convectively coupled equatorial waves within the MJO during CINDY/DYNAMO: slow Kelvin waves as building blocks. *Climate Dyn.,* **50,** 4211–4230, doi: 10.1007/s00382-017-3869-5.

Kiladis GN, Wheeler MC, Haertel PT, Straub KH, Roundy PE. 2009. Convectively coupled equatorial waves. *Rev. Geophys.,* **47,** RG2003, doi: 10.1029/2008RG000266.

Kiladis GN, Dias J, Gehne M, 2016: The relationship between equatorial mixed Rossby-gravity and eastward inertio-gravity waves. Part I. *J. Atmos. Sci.,* **73,** 2123–2145, doi: 10.1175/JAS-D-15-0230.1.

Latos B, Lefort T, Flatau MK, Flatau PJ, Permana DS, Baranowski CB, Paski JAI, Makmur E, Sulystyo K, Peyrille P, Feng Z, Matthews AJ, Schmidt JM, 2021. Equatorial waves triggering extreme rainfall and floods in southwest Sulawesi, Indonesia. *Mon. Weath. Rev.,* **149,** 1381–1401, doi: 10.1175/MWR-D-20-0262.1.

Lubis SW, Respati MR, 2021. Impacts of convectively coupled equatorial waves on rainfall extremes in Java, Indonesia. *Int. J. Clim.,* **41,** 2418–2440, doi: 10.1002/joc.6967.

Maloney ED, Hartmann DL. 1998. Frictional moisture convergence in a composite lifecycle of the Madden–Julian oscillation. *J. Climate,* **11,** 2387–2403, doi: 10.1175/1520-0442(1998)011¡2387%3AFMCIAC¿2.0.CO%3B2.

Matsuno T. 1966. Quasi-geostrophic motions in the equatorial area. *J. Meteorol. Soc. Japan,* **44,** 25–42.

Mekonnen A, Thorncroft CD, Aiyyer AR, Kiladis GN. 2009. Convectively coupled Kelvin waves over tropical Africa during the boreal summer: Structure and variability. *J. Climate,* **21,** 6649–6667, doi: 10.1175/2008JCLI2008.1.

Peatman SC, Methven J, Woolnough SJ. 2018. Isolating the effects of moisture entrainment on convectively coupled equatorial waves in an aquaplanet GCM. *J. Atmos. Sci.,* **75,** 3139–3157, doi: 10.1175/JAS-D-18-0098.1.

Roundy PE. 2008. Analysis of convectively coupled Kelvin waves in the Indian Ocean MJO. *J. Atmos. Sci.,* **65,** 1342–1359, doi: 10.1175/2007JAS2345.1.

Roundy PE. 2012. Observed structure of convectively coupled waves as a function of equivalent depth: Kelvin waves and the Madden-Julian Oscillation. *J. Atmos. Sci.,* **69,** 2097–2106, doi: 10.1175/JAS-D-12-03.1.

Roundy PE, Schreck CJ, 2009. A combined wavenumber-frequency and time-extended EOF approach for tracking the progress of modes of large-scale organized tropical convection. *Quart. J. Roy. Meteorol. Soc.,* **135,** 161–173, doi: 10.1002/qj.356.

Sakaeda N, Kiladis G, Dias J. 2020. The diurnal cycle of rainfall and the convectively coupled equatorial waves over the Maritime Continent. *J. Climate,* **33,** 3307–3331, doi: 10.1175/JCLI-D-19-0043.1.

Straub KH, Haertel PT, Kiladis GN. 2010. An analysis of convectively coupled Kelvin waves in 20 WCRP CMIP3 global coupled climate models. *J. Climate,* **23,** 3031–3056, doi: 10.1175/2009JCLI3422.1.

Straub KH, Kiladis GN. 2002. Observations of a convectively coupled Kelvin wave in the eastern Pacific ITCZ. *J. Atmos. Sci.,* **59,** 30–53, doi: 10.1175/1520-0469(2002)059<0030:OOACCK>2.0.CO;2.

Straub KH, Kiladis GN. 2003. The observed structure of convectively coupled Kelvin waves: Comparison with simple models of coupled wave instability. *J. Atmos. Sci.,* **60,** 1655–1668, doi: 10.1175/1520-0469(2003)060<1655:TOSOCC>2.0.CO;2.

Takayabu YN, 1994. Large-scale cloud disturbances associated with equatorial waves. Part I: Spectral features of the cloud disturbances. *J. Meteorol. Soc. Japan,* **72,** 433–448, doi: 10.2151/jmsj1965.72.3_433.

Tulich SN, Kiladis GN. 2012. Squall lines and convectively coupled gravity waves in the Tropics: Why do most cloud systems propagate westwards? *J. Atmos. Sci.,* **69,** 2995–3012, doi: 10.1175/JAS-D-11-0297.1.

Tulich SN, Mapes BE, 2008: Multiscale convective wave disturbances in the tropics: Insights from a two-dimensional cloud-resolving model. *J. Atmos. Sci.,* **65,** 140–155, doi: 10.1175/2007JAS2353.1.

van der Wiel K, Matthews AJ, Stevens DP, Joshi M. 2015. A dynamical framework for the origin of the diagonal South Pacific and South Atlantic convergence zones. *Quart. J. Roy. Meteorol. Soc.,* **141,** 1997–2010, doi: 10.1002/qj.2508.

Veldman AEP, Rinzema K. 1992. Playing with nonuniform grids. *J. Eng. Math.,* **26,** 119–130.

Wang L, Li T, 2016. Convectively coupled Kelvin waves in CMIP5 coupled climate models. *Clim. Dyn.,* **48,** 767–781, doi: 10.1007/s00382-016-3109-4.

Wheeler M, Kiladis GN, Webster PJ. 2000. Large-scale dynamical fields associated with convectively coupled equatorial waves. *J. Atmos. Sci.,* **57,** 613–640, doi: 10.1175/1520-0469(2000)057<0613:LSDFAW>2.0.CO;2.

Wheeler M, Kiladis GN. 1999. Convectively coupled equatorial waves: Analysis of clouds and temperature in the wavenumber-frequency domain. *J. Atmos. Sci.,* **56,** 374–399, doi: 10.1175/1520-0469(1999)056<0374:CCEWAO>2.0.CO;2.

Yang GY, Hoskins BJ, Slingo JM. 2003. Convectively coupled equatorial waves: A new methodology for identifying wave structures in observational data. *J. Atmos. Sci.,* **60,** 1637–1654, doi: 10.1175/1520-0469(2003)060<1637:CCEWAN>2.0.CO;2.

Yang GY, Hoskins BJ, Slingo JM. 2007a. Convectively coupled equatorial waves. Part I: Horizontal and vertical structures. *J. Atmos. Sci.,* **64,** 3406–3423, doi: 10.1175/JAS4017.1.

Yang GY, Hoskins BJ, Slingo JM. 2007b. Convectively coupled equatorial waves. Part II: Propagation characteristics. *J. Atmos. Sci.,* **64,** 3424–3437, doi: 10.1175/JAS4018.1.

Yang G-Y, Ferrett S, Woolnough S, Methven J, Holloway C. 2021. Real-time identification of equatorial waves and evaluation of waves in global forecasts. *Weath. Forecast.,* **36,** 171–193, doi: 10.1175/WAF-D-20-0144.1.

Yang GY, Hoskins BJ, Slingo JM. 2007c. Convectively coupled equatorial waves. Part III: Synthesis structures and their forcing and evolution. *J. Atmos. Sci.,* **64,** 3438–3451, doi: 10.1175/JAS4019.1.

Zagar N, Andersson E, Fisher M, 2005. Balanced tropical data assimilation based on a study of equatorial waves in ECMWF short-range forecast errors. *Quart. J. Roy. Meteorol. Soc.,* **131,** 987–1011, doi: 10.1256/qj.04.54.

Table 1. Behaviour of growth and wave propagation, depending on value of phase difference θ between vorticity and vorticity source term

Phase θ	Behaviour
$-\frac{\tau}{2} < \theta < -\frac{\tau}{4}$	Mixture of decay and westward propagation
$\theta = -\frac{\tau}{4}$	No growth, pure westward propagation
$-\frac{\tau}{4} < \theta < 0$	Mixture of decay and westward propagation
$\theta = 0$	Pure growth, no propagation
$0 < \theta < \frac{\tau}{4}$	Mixture of growth and eastward propagation
$\theta = \frac{\tau}{4}$	No growth, pure eastward propagation
$\frac{\tau}{4} < \theta < \frac{\tau}{2}$	Mixture of decay and eastward propagation
$\theta = \frac{\tau}{2}$	Pure decay, no propagation

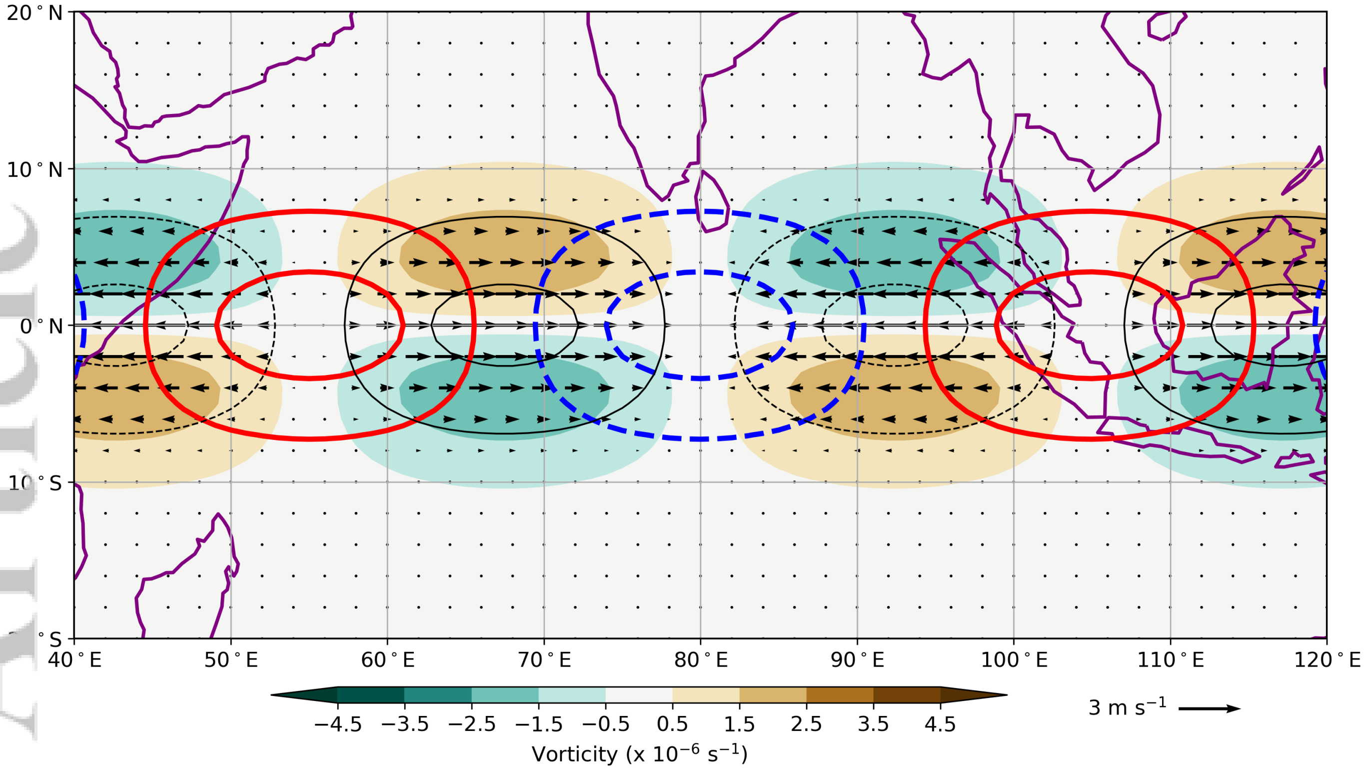

Figure 1. Structure of a sample theoretical linear equatorial Kelvin wave with zonal wavelength 5,820 km ($k = 1.08 \times 10^{-6}$ m^{-1}), trapping scale $y_0 = 690$ km (corresponding to a phase speed $c_e = 5.5$ m s^{-1}), and amplitude $u_0 = 1.8$ m s^{-1}. Horizontal wind vectors are shown by the black arrows (scale vector has length 3 m s^{-1}). Zonal wind speed is shown by the thin black line contours; interval is 1 m s^{-1}, positive contours are solid and the first positive contour is at 0.5 m s^{-1}, negative contours are dashed. Relative vorticity is colour shaded, with interval 1×10^{-6} s^{-1}; first positive contour is at 0.5×10^{-6} s^{-1}. Divergence is shown by the thick line contours with interval 1×10^{-6} s^{-1}; positive contours are solid red and first positive contour is at 0.5×10^{-6} s^{-1}, negative contours are blue dashed. Continental outlines are shown in purple for scale only.

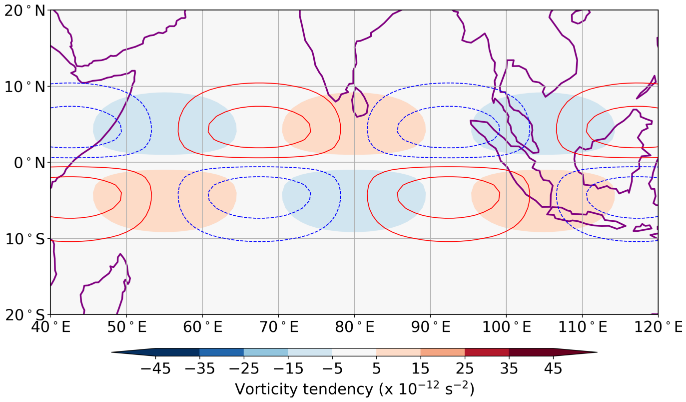

Figure 2. Vorticity tendency (equal to total vorticity source $-fD$) of the theoretical linear equatorial Kelvin wave in Figure 1. Colour shading interval is 10×10^{-12} s^{-2}; first positive level is at 5×10^{-12} s^{-2}. The vorticity anomaly is shown by line contours; interval is 1×10^{-6} s^{-1}, positive contours are solid red and first positive contour is at 0.5×10^{-6} s^{-1}, and negative contours are dashed blue.

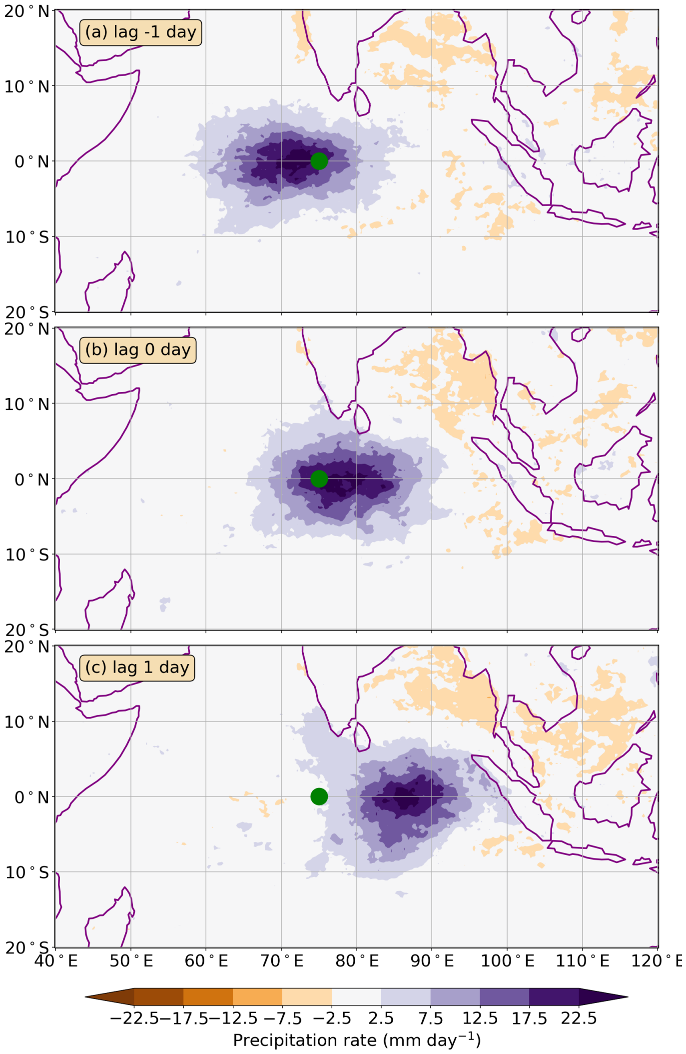

Figure 3. Lagged composite maps of TRMM precipitation anomalies of CCKW, with basepoint at 75°E (indicated by the green circle), for day: (a) -1, (b) 0, (c) 1. Colour shading interval is 5 mm day^{-1}.

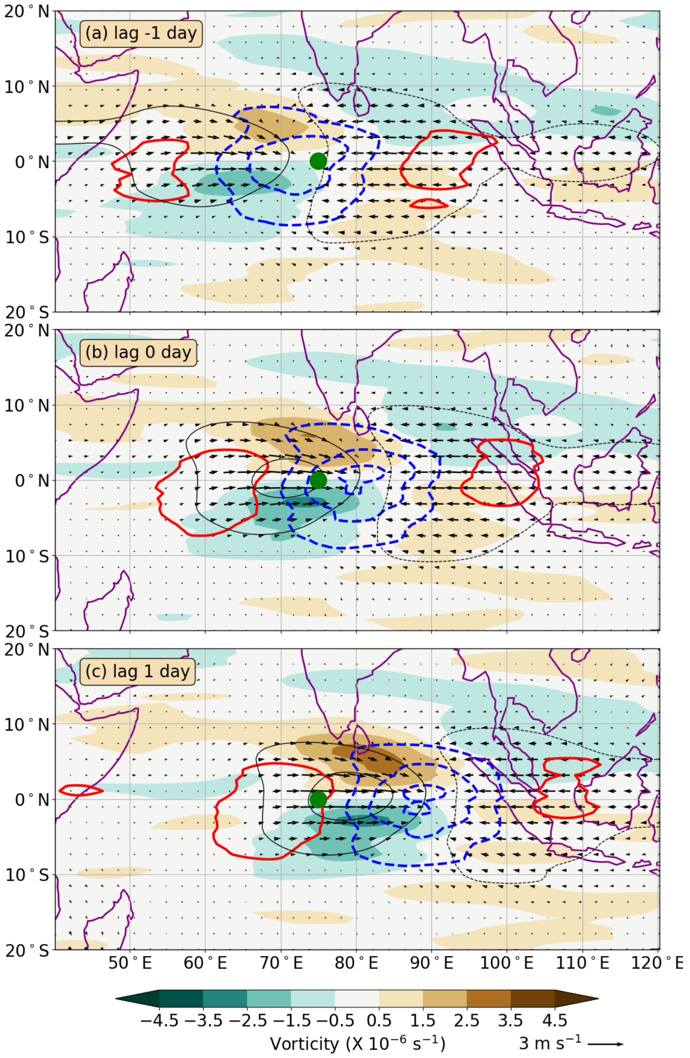

Figure 4. Lagged composite maps of dynamical anomalies of CCKW at 850 hPa, for day: (a) −1, (b) 0, (c) 1. Horizontal wind vectors are shown by the black arrows (scale vector has length 3 m s^{-1}). Zonal wind speed is shown by the thin black line contours; interval is 1 m s^{-1}, positive contours are solid and first positive contour is at 0.5 m s^{-1}, negative contours are dashed. Relative vorticity is colour shaded, with interval 1×10^{-6} s^{-1}; first positive contour is at 0.5×10^{-6} s^{-1}. Divergence is shown by the thick line contours with interval 1×10^{-6} s^{-1}; positive contours are solid red and first positive contour is at 0.5×10^{-6} s^{-1}, negative contours are blue dashed.

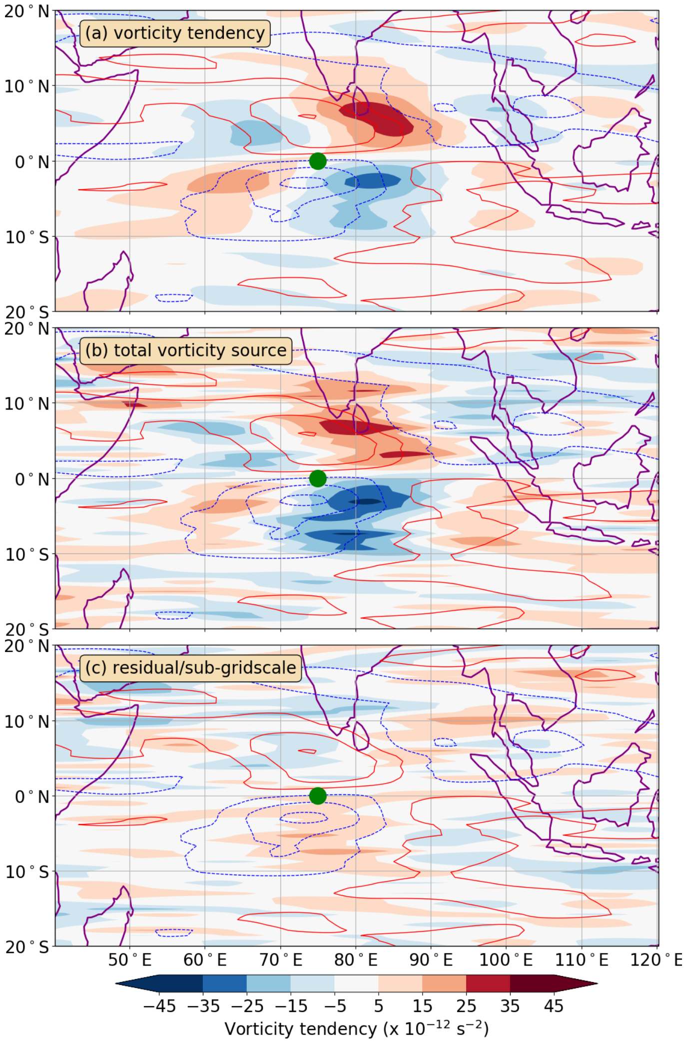

Figure 5. Zero-lagged composite maps of basic vorticity budget of CCKW at 850 hPa: (a) vorticity tendency, (b) total vorticity source, (c) residual/sub-gridscale processes. Contour shading interval is 10×10^{-12} s^{-2}; the first positive contour is at 5×10^{-12} s^{-2}. The vorticity anomaly is shown by line contours in each panel; interval is 1×10^{-6} s^{-1}, positive contours are solid red and first positive contour is at 0.5×10^{-6} s^{-1}, and negative contours are dashed blue.

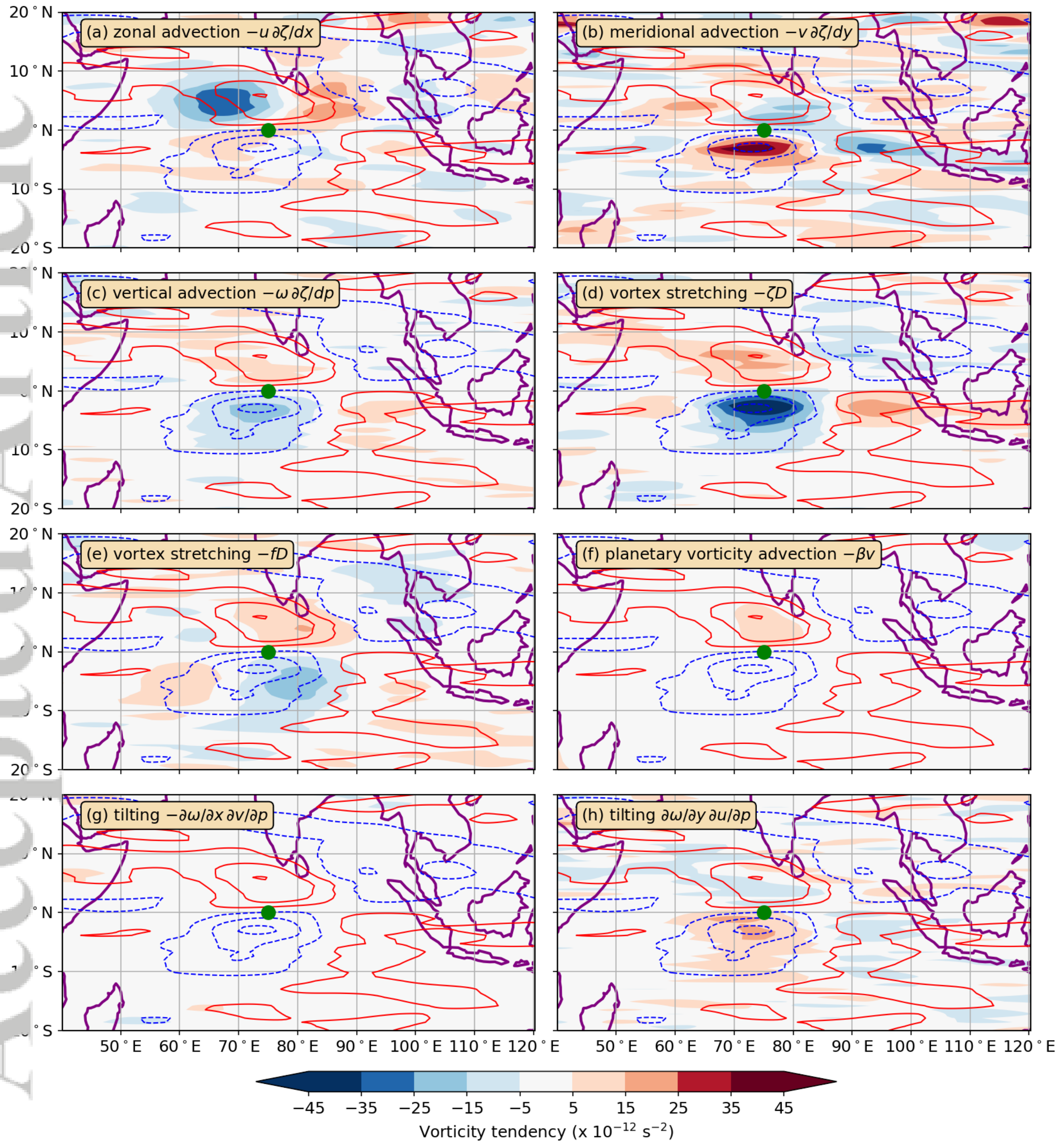

Figure 6. Zero-lagged composite maps of individual source terms in vorticity budget of CCKW at 850 hPa: (a) zonal advection $-u\partial\zeta/\partial x$, (b) meridional advection $-v\partial\zeta/\partial y$, (c) vertical advection $-\omega\partial\zeta/\partial p$, (d) vortex stretching $-\zeta D$, (e) vortex stretching $-fD$, (f) planetary vorticity advection $-\beta v$, (g) tilting $-\partial\omega/\partial x\,\partial v/\partial p$, (h) tilting $\partial\omega/\partial y\,\partial u/\partial p$. Conventions as in Figure 5.

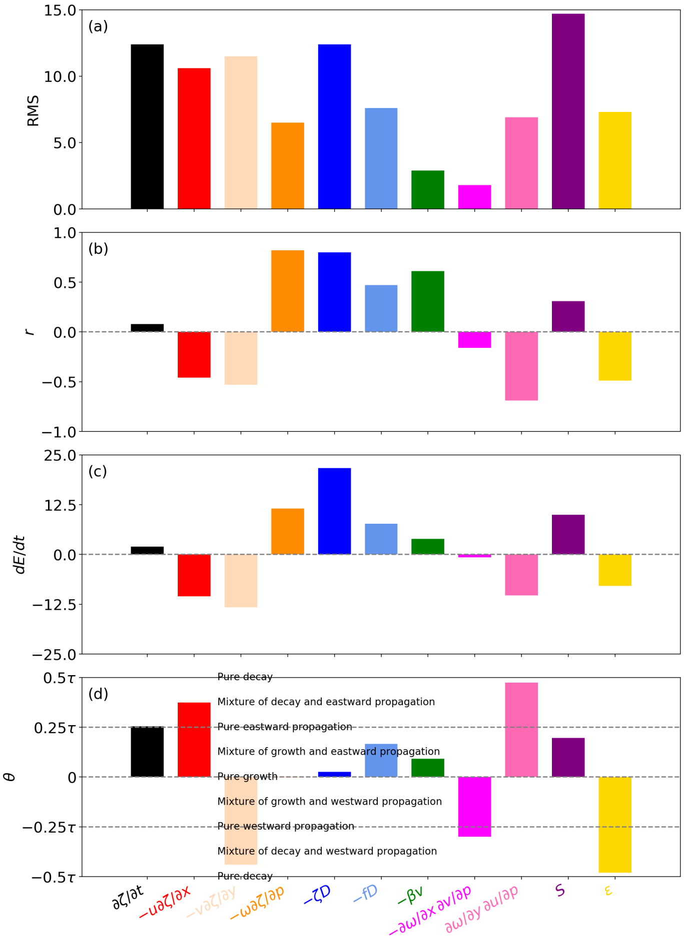

Figure 7. Diagnostics of vorticity source terms at 850 hPa calculated from zero lag composite fields over the domain 55–95°E, 10°S–10°N: (a) RMS amplitude ($\times 10^{-12}$ s^{-2}), (b) spatial correlation coefficient r, (c) enstrophy tendency $\partial E/\partial t$ ($\times 10^{-18}$ s^{-3}), (d) phase difference θ between vorticity anomaly field and vorticity source term (multiple of τ, i.e., fraction of a turn).

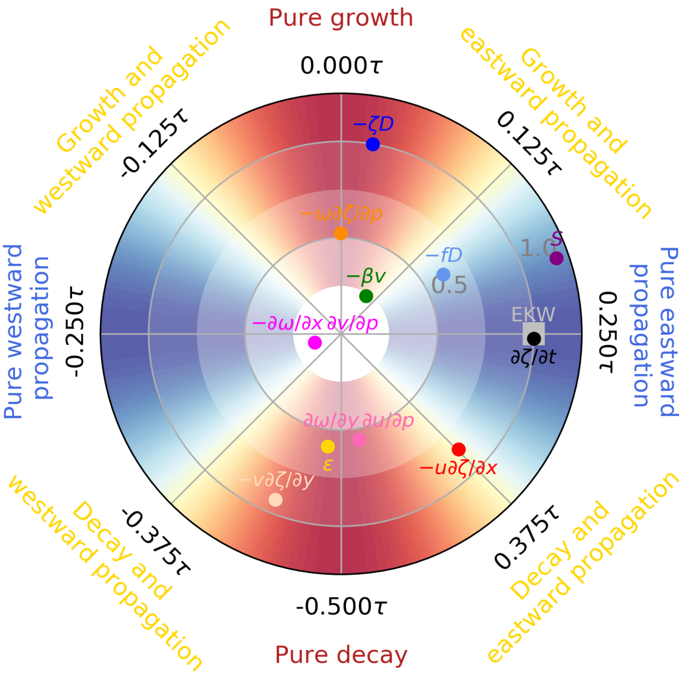

Figure 8. Vorticity budget propagation–growth polar diagram of 850-hPa CCKW vorticity source terms, with normalised RMS amplitude as the radial coordinate, and phase difference θ between the source term and the vorticity anomaly, as the azimuthal coordinate. Contrary to regular convention, the azimuthal coordinate axis is zero on the positive vertical axis, and increases in a clockwise direction. This enables growth to be toward the top of the diagram, decay to the bottom, westward propagation to the left, and eastward propagation to the right. The single $(-fD)$ source term for a theoretical equatorial Kelvin wave is shown by the large grey square, labelled "EKW".

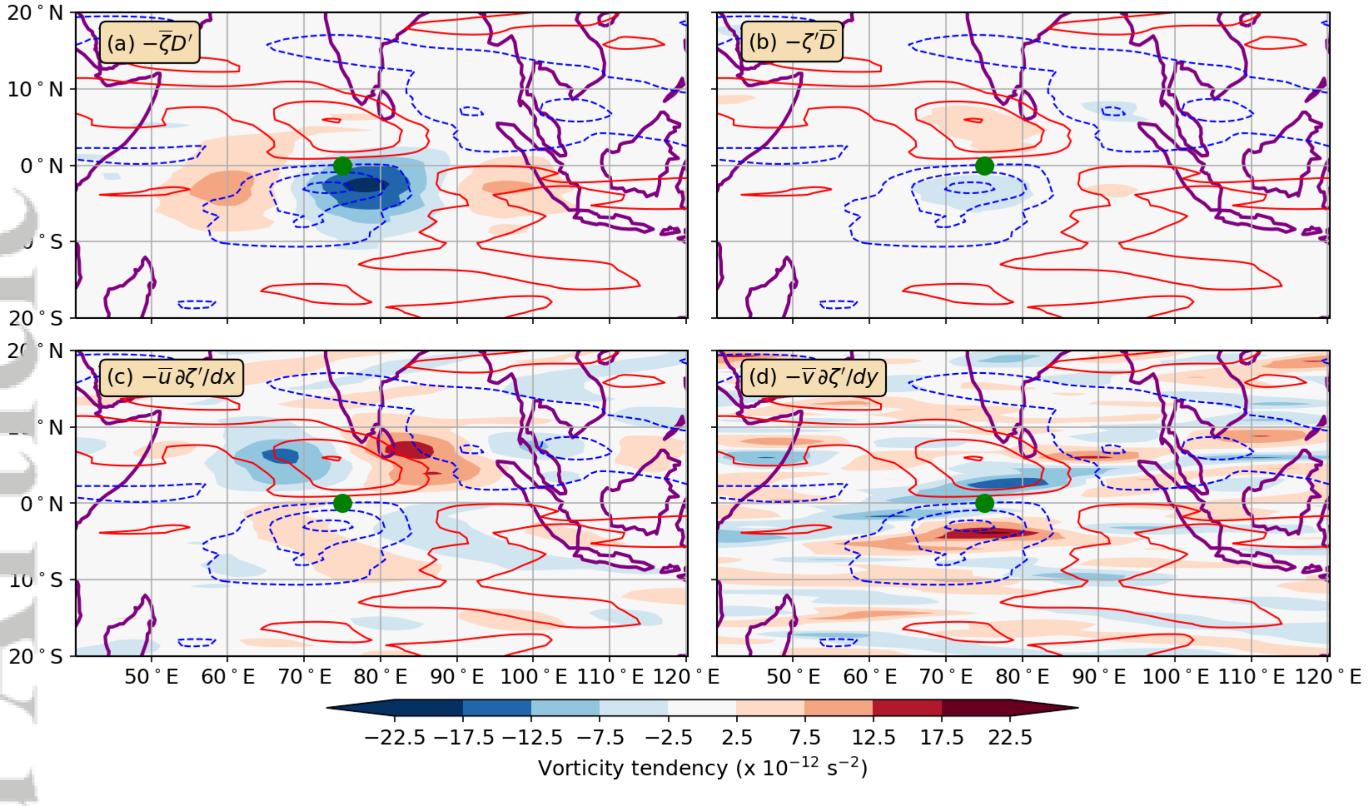

Figure 9. Decomposition of selected vorticity sources at 850 hPa into contributions from the basic state and perturbation fields. Zero-lagged composite maps of: (a) $-\overline{\zeta}D'$, (b) $-\zeta'\overline{D}$, (c) $-\overline{u}\partial\zeta'/\partial x$, (d) $-\overline{v}\partial\zeta'/\partial y$. Conventions as in Figure 5.

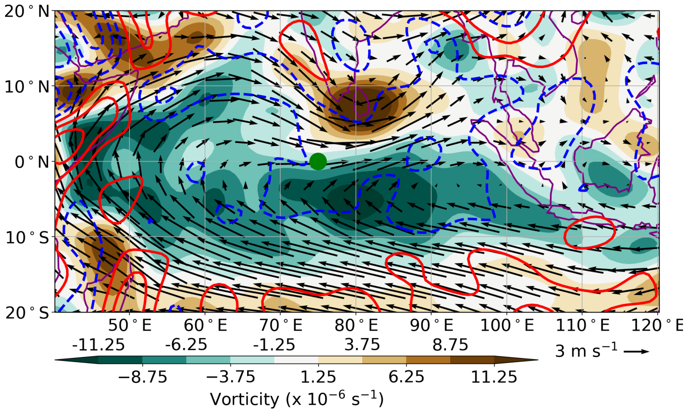

Figure 10. Zero-lagged composite map of the background 850-hPa wind vectors $(\overline{u}, \overline{v})$, vorticity $(\overline{\zeta})$ and divergence $(\overline{D})$. Horizontal wind vectors are shown by the black arrows (scale vector has length 3 m s^{-1}). Relative vorticity is colour shaded, with interval 2.5×10^{-6} s^{-1}; first positive contour is at 1.25×10^{-6} s^{-1}. Divergence is shown by the thick line contours with interval 2×10^{-6} s^{-1}; positive contours are solid red and first positive contour is at 1×10^{-6} s^{-1}, negative contours are blue dashed.

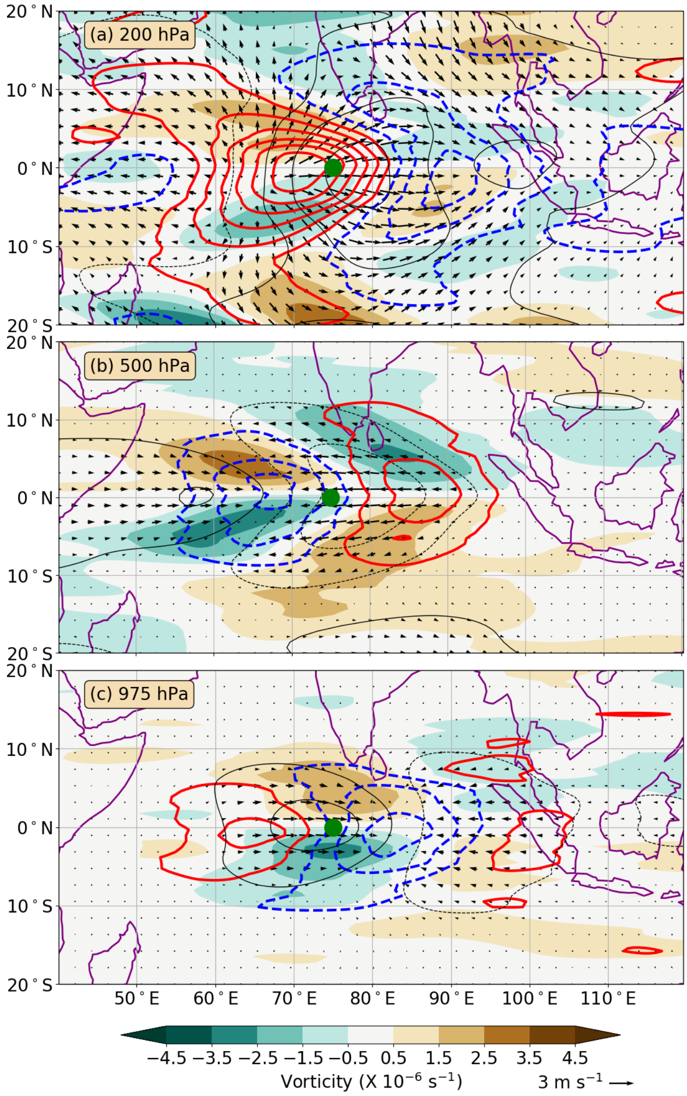

Figure 11. Zero-lagged composite maps of dynamical anomalies of CCKW at (a) 200, (b) 500, (c) 975 hPa. Conventions as in Figure 4.

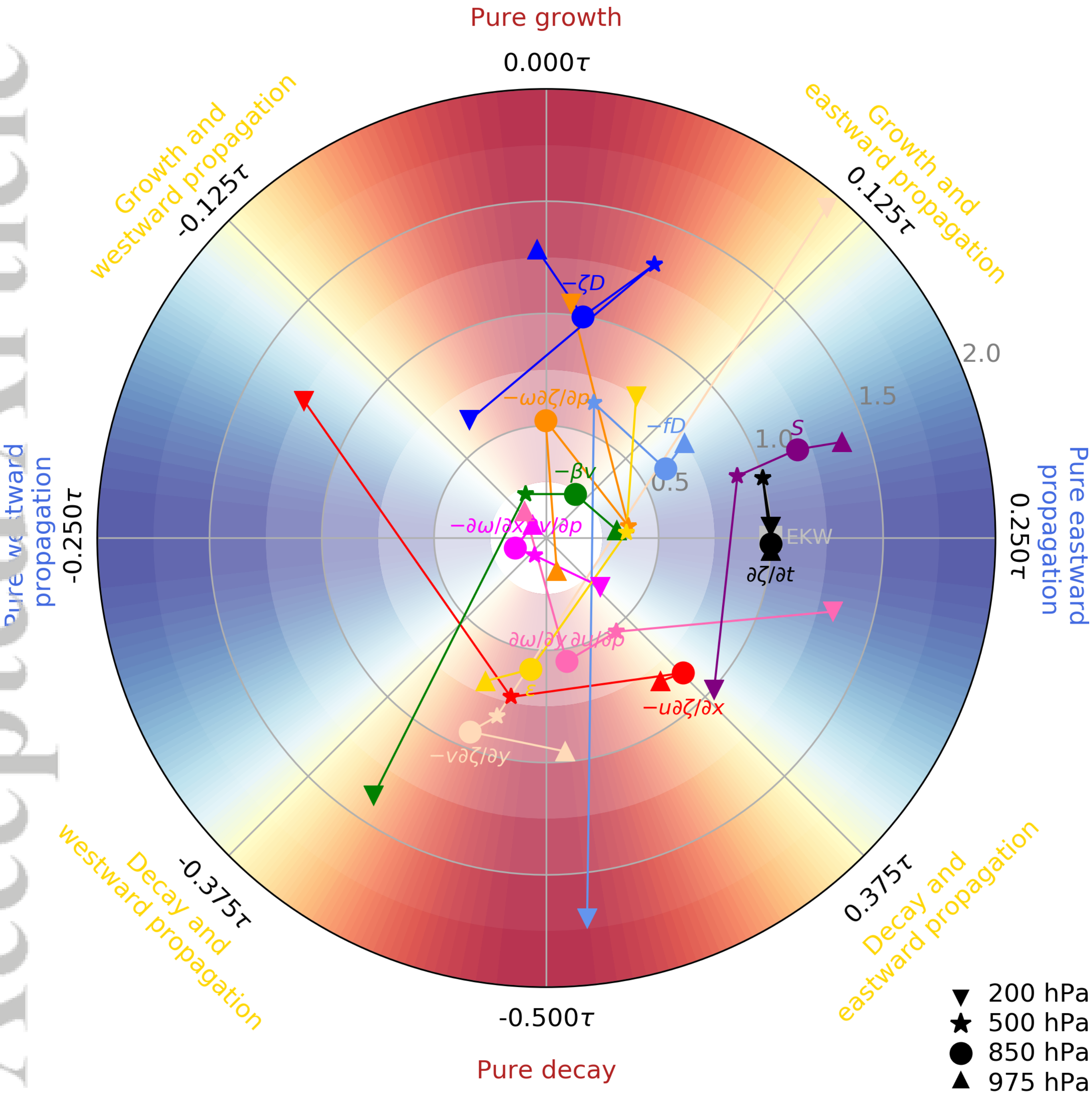

Figure 12. As Figure 8 but for multiple levels. Each source term is shown by a marker for each level (see key), joined by a line of the appropriate colour, forming a “constellation” pattern. Note that the radial axis is expanded, compared with the single level version in Figure 8.